

Impacts of short-term mitigation measures on PM_{2.5} and radiative effects: case study at a regional background site near Beijing, China

Qiyuan Wang^{1*}, Suixin Liu¹, Nan Li², Wenting Dai¹, Yunfei Wu³, Jie Tian⁴, Yaqing Zhou¹, Meng Wang¹, Steven Sai Hang Ho¹, Yang Chen⁵, Renjian Zhang³, Shuyu Zhao¹, Chongshu Zhu¹, Yongming Han^{1,6}, Xuexi Tie¹, Junji Cao^{1,7*}

¹Key Laboratory of Aerosol Chemistry and Physics, State Key Laboratory of Loess and Quaternary Geology, Institute of Earth Environment, Chinese Academy of Sciences, Xi'an, 710061, China.

²School of Environmental Science and Engineering, Nanjing University of Information Science & Technology, Nanjing, 210044, China

³Key Laboratory of Regional Climate-Environment Research for Temperate East Asia, Institute of Atmospheric Physics, Chinese Academy of Sciences, Beijing, 100029, China.

⁴Department of Environmental Science and Engineering, School of Energy and Power Engineering, Xi'an Jiaotong University, Xi'an 710049, China.

⁵Chongqing Institute of Green and Intelligent Technology, Chinese Academy of Sciences, Chongqing 400714, China.

⁶School of Human Settlements and Civil Engineering, Xi'an Jiaotong University, Xi'an, 710049, China.

⁷Institute of Global Environmental Change, Xi'an Jiaotong University, Xi'an, 710049, China.

Correspondence to: Qiyuan Wang (wangqy@ieecas.cn) and Junji Cao (cao@loess.llqg.ac.cn)

Abstract. Measurements at a background site near Beijing showed that pollution controls implemented during the 19th National Congress of the Communist Party of China (NCCPC) were effective in reducing PM_{2.5}. Mass concentrations of PM_{2.5} and its major chemical components were 20.6–43.1% lower during the NCCPC-control period compared with a non-control period, and differences were greater on days with stable meteorological conditions. A receptor model showed that PM_{2.5} from traffic-related emissions, biomass burning, industrial processes, and mineral dust was 38.5–77.8% lower during the NCCPC-control versus non-control period, but differences in PM_{2.5} from coal burning were small, and secondary source was higher during the control period. During one pollution episode in the non-control period, secondary source dominated, and the WRF-Chem model showed that the Beijing-Tianjin-Hebei (BTH) region contributed 73.6% of PM_{2.5} mass. A second pollution episode was linked to biomass burning, and BTH contributed 46.9% of PM_{2.5} mass. Calculations based on IMPROVE algorithms showed that organic matter was the largest contributor to light extinction during the non-control period whereas NH₄NO₃ was the main contributor during the NCCPC. The Tropospheric Ultraviolet and Visible radiation model showed that the average direct radiative forcing (DRF) values at the Earth's surface were -14.0 and -19.3 W m⁻² during the NCCPC-control and non-control periods, respectively, and the DRF for the individual PM_{2.5} components were 22.7–46.7% lower during the NCCPC. The information and dataset from this

35 study will be useful for developing air pollution control strategies in the BTH region and for
36 understanding associated aerosol radiative effects.

37 **1 Introduction**

38 High loadings of fine particulate matter (PM_{2.5}, particulate matter with an aerodynamic diameter ≤ 2.5
39 μm) cause air quality to deteriorate (Pui et al., 2014; Tao et al., 2017), reduce atmospheric visibility
40 (Watson, et al., 2002; Cao et al., 2012), and adversely affect human health (Feng et al., 2016; Xie et al.,
41 2016). Moreover, PM_{2.5} can directly and indirectly affect climate and ecosystems (Lecoeur et al., 2014;
42 Tie et al., 2016). With the rapid increases in economic growth, industrialization, and urbanization in the
43 past two decades, Beijing has experienced serious PM_{2.5} pollution, especially in winter (e.g., Zhang et al.,
44 2013; Elser et al., 2016; Wang et al., 2016a; Zhong et al., 2018). Since the Chinese government
45 promulgated the National Ambient Air Quality Standards for PM_{2.5} in 2012 (NAAQS, GB3095–2012), a
46 series of emission control strategies have been implemented in Beijing and surrounding areas to alleviate
47 the serious air pollution problems. These measures include installing desulphurization systems in coal-
48 fired power plants, banning high-emission motor vehicles, and promoting natural gas as an alternative to
49 coal in rural areas. According to the China Environmental State Bulletin
50 (www.zhb.gov.cn/hjzl/zghjzkqb/lnzghjzkqb, in Chinese), the annual levels of PM_{2.5} during 2013–2016 in
51 Beijing showed a decreasing trend ($r = 0.98$ and slope = $-5.3 \mu\text{g m}^{-3} \text{ year}^{-1}$), but there were still 45.9% of
52 days in 2016 that suffered from varying degrees of pollution.

53 Identifying the causes of air pollution in Beijing is challenging because the chemical composition of PM_{2.5}
54 is variable and complex, and the particles originate from a variety of sources and processes. For example,
55 Elser et al. (2016) reported that organic aerosol (OA) was the largest contributor to PM_{2.5} mass during
56 extreme haze periods in Beijing, and the primary aerosol from coal combustion (46.8%) was the dominant
57 contributor to OA, followed by the oxygenated OA (25.0%) and biomass burning OA (13.8%). In addition,
58 Zheng et al. (2016) found that organic matter (OM) was the most abundant component (18–60%) in PM_{2.5},
59 but its relative contribution usually decreased as pollution levels rose while those of secondary inorganic
60 species (e.g., sulfate and nitrate) increased.

61 In recent years, the Chinese government has taken temporary control measures to ensure good air quality
62 during some important conferences and festivals held in Beijing, including the 2008 Summer Olympic
63 Games, the 2014 Asia-Pacific Economic Cooperation (APEC) summit, and the 2015 Victory Day parade
64 (VDP). These actions provide valuable opportunities for evaluating the effectiveness of emission controls

65 on air pollution, and the information gathered during the control periods should be useful for making policy
66 decisions. Numerous studies have demonstrated that temporary aggressive control measures were
67 effective in reducing primary pollutants and secondary aerosol formation in Beijing (e.g., Wang et al.,
68 2010; Guo et al., 2013; Li et al., 2015; Tao et al., 2016; Xu et al., 2017).

69 Air pollution in Beijing is not only influenced by local emissions and the regional transport of pollutants
70 but also by meteorological conditions (e.g., Li and Han, 2016; Bei et al., 2017). In this regard, Zhong et
71 al. (2018) concluded that heavy pollution episodes in Beijing can be generally divided into two phases (1)
72 a transport stage, which is characterized by increases in pollutants mainly transported from the south of
73 Beijing and (2) an accumulation stage, during which there is dramatic growth in PM_{2.5} loadings due to
74 stagnant meteorological conditions. Moreover, several studies showed that the emission controls put in
75 place during important events were effective in decreasing aerosol concentrations, but meteorological
76 conditions also played an important role in determining aerosol loadings (Gao et al., 2011; Liang et al.,
77 2017). For example, Liang et al. (2017) found that meteorological conditions and emission control
78 measures had comparable impacts on PM_{2.5} loadings in Beijing during the 2014 APEC (30% versus 28%,
79 respectively) and the 2015 VDP (38% versus 25%).

80 The existing studies on the effects of temporary air pollution controls in Beijing have not covered mid-
81 autumn when meteorological conditions are typically complex and variable. Indeed, Zhang et al. (2018)
82 reported that two weather patterns common in October caused heavy pollution episodes in Beijing. One
83 episode was linked to a Siberian high-pressure system and a uniform high-pressure field while the second
84 was associated with a cold front and a low-pressure system. For this study, measurements were made at
85 a regional background site in the Beijing-Tianjin-Hebei (BTH) region to investigate the changes of PM_{2.5}
86 during the 19th National Congress of the Communist Party of China (NCCPC), which was held in Beijing
87 from 18–24 October. Temporary control measures were implemented in Beijing and neighboring areas;
88 these included restrictions on the number of vehicles, prohibition of construction activities, and
89 restrictions on factories and industrial production. The primary objectives of this study were to (1)
90 investigate the effectiveness of emission control measures on PM_{2.5} and the associated changes in its
91 chemical composition; (2) determine the contributions of emission sources to PM_{2.5} mass during the
92 NCCPC-control and non-control periods; and (3) evaluate the impacts of reductions of PM_{2.5} on aerosol
93 direct radiative forcing (DRF) at the Earth's surface. The study produced a valuable dataset and the results
94 provide insights into how controls on air pollution can affect Beijing.

95 **2 Materials and methods**

96 **2.1 Sampling site**

97 Intensive measurements were made from 12 October to 4 November 2017 at the Xianghe Atmospheric
98 Observatory (39.75° N, 116.96° E; 36 m above sea level) to investigate how the characteristics of PM_{2.5}
99 and the associated radiative effects were affected by the controls put in place during the NCCPC. Xianghe
100 is a small county with 0.33 million residents, and it is located in a major plain-like area ~50 km southeast
101 from Beijing and ~70 km north from Tianjin (Figure 1). The sampling site is surrounded by residential
102 areas and farmland, and it is ~5 km west of Xianghe city center. This regional aerosol background site is
103 influenced by mixed emission sources in the BTH region. A more detailed description of the site may be
104 found in Ran et al. (2016).

105 **2.2 Measurements**

106 **2.2.1 Offline measurements**

107 PM_{2.5} samples were collected on 47 mm quartz-fiber filters (QM/A; GE Healthcare, Chicago, IL, USA)
108 and Teflon[®] filters (Whatman Limited, Maidstone, UK) using two parallel mini-volume samplers
109 (Airmetrics, Oregon, USA) that operated at a flow rate of 5 L min⁻¹. The duration of sampling was 24 h,
110 and the sampling interval was from 09:00 local time to 09:00 the next day. To minimize the evaporation
111 of volatile materials, the samples were stored in a refrigerator at -4 °C before the chemical analyses. The
112 quartz-fiber filters were used for determinations of water-soluble inorganic ions and carbonaceous species
113 while the Teflon[®] filters were used for inorganic elemental analyses. The PM_{2.5} mass on each sample
114 filter was determined gravimetrically using a Sartorius MC5 electronic microbalance with ± 1 µg
115 sensitivity (Sartorius, Göttingen, Germany). For the mass determinations, the filters were equilibrated
116 under controlled temperature (20–23 °C) and relative humidity (35–45%) before the measurements were
117 made. Field blanks (a blank quartz-fiber filter and a blank Teflon[®] filter) were collected and analysed to
118 account for possible background effects.

119 Water-soluble inorganic ions, including F⁻, Cl⁻, NO₃⁻, SO₄²⁻, Na⁺, K⁺, Mg²⁺, Ca²⁺, and NH₄⁺ were
120 measured with the use of a Dionex 600 ion chromatograph (IC, Dionex Corp., Sunnyvale, CA, USA).
121 The four anions of interest were separated using an ASII-HC column (Dionex Corp.) and 20 mM
122 potassium hydroxide as the eluent. The five cations were separated using a CS12A column (Dionex) and
123 an eluent of 20 mM methane sulfonic acid. More detailed description of the IC analyses may be found in
124 Zhang et al. (2011). Carbonaceous species, including organic carbon (OC) and elemental carbon (EC)

125 were determined using a Desert Research Institute (DRI) Model 2001 thermal/optical carbon analyzer
126 (Atmoslytic Inc., Calabasa, CA, USA) following the Interagency Monitoring of Protected Visual
127 Environments (IMPROVE_A) protocol (Chow et al., 2007). A standard sucrose solution was used to
128 establish a standard carbon curve before the analytical runs. Replicate analyses were performed at a rate
129 of one sample for every ten samples, and the repeatability was found to be < 15% for OC and < 10% for
130 EC. More information of the OC and EC measurement procedures may be found in Cao et al. (2003).
131 Thirteen elements were determined by energy-dispersive X-ray fluorescence (ED-XRF) spectrometry
132 (Epsilon 5 ED-XRF, PANalytical B.V., Netherlands), and these elements include Al, Si, K, Ca, Ti, Cr,
133 Mn, Fe, Cu, Zn, As, Br, and Pb. The analytical accuracy for ED-XRF measurements was determined with
134 a NIST Standard Reference Material 2783 (National Institute of Standards and Technology, Gaithersburg,
135 MD, USA). A more detailed description of the ED-XRF methods may be found in Xu et al. (2012).

136 **2.2.2 Online measurements**

137 The aerosol optical properties were determined using a Photoacoustic Extinctionmeter (PAX, Droplet
138 Measurement Technologies, Boulder, CO, USA) at a wavelength of 532 nm. The PAX measured light
139 scattering (b_{scat}) and absorption (b_{abs}) coefficients (in Mm^{-1}) simultaneously using a built-in wide-angle
140 integrating reciprocal nephelometer and a photoacoustic technique, respectively. Before and during the
141 sampling, the PAX b_{scat} and b_{abs} were calibrated using ammonium sulfate and fullerene soot particles,
142 respectively, which were generated with an atomizer (Model 9302, TSI Inc., Shoreview, MN, USA).
143 Detailed calibration procedures have been described in Wang et al. (2018a; 2018b). For this study, the
144 PAX was fitted with a $\text{PM}_{2.5}$ cutoff inlet, and the sampled particles were dried by a Nafion® dryer (MD-
145 700-24S-1; Perma Pure, LLC., Lakewood, NJ, USA). The time resolution of the data logger was set to 1
146 minute.

147 One-minute average mixing ratios of NO_x ($\text{NO} + \text{NO}_2$), O_3 , and SO_2 were measured using a Model 42i
148 gas-phase chemiluminescence NO_x analyzer (Thermo Fisher Scientific, Inc., Waltham, MA, USA), a
149 Model 49i photometric ozone analyzer (Thermo Fisher Scientific, Inc.), and a Model 43i pulsed UV
150 fluorescence analyzer (Thermo Fisher Scientific, Inc.), respectively. Standard reference NO , O_3 , and SO_2
151 gases were used to calibrate the NO_x , O_3 , and SO_2 analyzers, respectively, before and during the campaign.
152 All the online data were averaged to 24 h and matched to the duration of the filter sampling.

153 2.2.3 Complementary data

154 Wind speed (WS) and relative humidity (RH) were measured with the use of an automatic weather station
155 installed at the Xianghe Atmospheric Observatory. Surface weather charts for East Asia were obtained
156 from the Korea Meteorological Administration. The three-day backward in time trajectories and mixed
157 layer heights (MLHs) were calculated using the Hybrid Single-Particle Lagrangian Integrated Trajectory
158 (HYSPLIT) model (Draxler and Rolph, 2003), which was developed by the National Oceanic and
159 Atmospheric Administration (NOAA). The aerosol optical depth (AOD) was measured using a
160 sunphotometer (Cimel Electronique, Paris, France), and those data were obtained from the Aerosol
161 Robotic Network data archive (<http://aeronet.gsfc.nasa.gov>). Fire counts were obtained from the
162 Moderate Resolution Imaging Spectroradiometer (MODIS) instruments on the Aqua and Terra satellites
163 (<https://firms.modaps.eosdis.nasa.gov/map>).

164 2.3 Data analysis methods

165 2.3.1 Chemical mass closure

166 The chemically reconstructed PM_{2.5} mass was calculated as the sum of OM, EC, SO₄²⁻, NO₃⁻, NH₄⁺, Cl⁻,
167 fine soil, and trace elements. A factor of 1.6 was used to convert OC to OM (OM = 1.6 × OC) to account
168 for those unmeasured atoms in organic materials based on the results of Xu et al. (2015). The mass
169 concentration of fine soil was calculated by summing the masses of Al, Si, K, Ca, Ti, Mn, and Fe oxides
170 using the following equation (Cheung et al., 2011):

$$\begin{aligned} 171 \text{ [Fine soil]} &= [\text{Al}_2\text{O}_3] + [\text{SiO}_2] + [\text{K}_2\text{O}] + [\text{CaO}] + [\text{TiO}_2] + [\text{MnO}_2] + [\text{Fe}_2\text{O}_3] \\ 172 &= 1.89 \times [\text{Al}] + 2.14 \times [\text{Si}] + 1.21 \times [\text{K}] + 1.4 \times [\text{Ca}] + 1.67 \times [\text{Ti}] + 1.58 \times [\text{Mn}] + 1.43 \times [\text{Fe}] \end{aligned} \quad (1)$$

173 The mass concentration of trace elements was calculated as the sum of measured elements that were not
174 used in the calculation of fine soil:

$$175 \text{ [Trace elements]} = [\text{Cr}] + [\text{Cu}] + [\text{Zn}] + [\text{As}] + [\text{Br}] + [\text{Pb}] \quad (2)$$

176 As shown in Figure S1, the reconstructed PM_{2.5} mass was strongly correlated ($r = 0.98$) with the
177 gravimetrically determined values, and this attests to the validity of the chemical reconstruction method.
178 The slope of 0.86 indicates that our measured chemical species accounted for most of the PM_{2.5} mass.
179 The difference between the reconstructed and measured PM_{2.5} mass was defined as “others”.

180 2.3.2 Receptor model source apportionment

181 Positive matrix factorization (PMF) has been widely used in source apportionment studies in the past two
182 decades (e.g., Cao et al., 2012; Xiao et al., 2014; Tao et al., 2014; Huang et al., 2017). The principles of
183 PMF are described in detail elsewhere (Paatero and Tapper, 2006). Briefly, PMF is a bilinear factor model
184 that decomposes an initial chemically-specified dataset into a factor contribution matrix G_{ik} ($i \times k$
185 dimensions) and a factor profile matrix F_{kj} ($k \times j$ dimensions) and then iteratively minimizes the object
186 function Q :

$$187 X_{ij} = \sum_{k=1}^p G_{ik} F_{kj} + E_{ij} \quad (3)$$

$$188 Q = \sum_{i=1}^m \sum_{j=1}^n \left(\frac{E_{ij}}{\sigma_{ij}} \right)^2 \quad (4)$$

189 where X_{ij} is the concentration of the j th species measured in the i th sample; E_{ij} is the model residual; and
190 σ_{ij} represents the uncertainty.

191 In this study, the PMF Model version 5.0 (PMF 5.0) from US Environmental Protection Agency (EPA)
192 (Norris et al., 2014) was employed to identify the $PM_{2.5}$ sources. Four to nine factors were extracted to
193 determine the optimal number of factors with random starting points. When the values of scaled residuals
194 for all chemical species varied between -3 and +3 and a small $Q_{\text{true}}/Q_{\text{expect}}$ was obtained, the base run was
195 considered to be stable. Further, bootstrap analysis (BS), displacement analysis (DISP), and bootstrap-
196 displacement analysis (BS-DISP) were applied to assess the variability and stability of the results. A more
197 detailed description of the methods for the determination of uncertainties in PMF solutions can be found
198 in Norris et al. (2014).

199 2.3.3 Regional chemical dynamical model

200 The Weather Research and Forecasting model coupled to chemistry model (WRF-Chem) is a 3-D online-
201 coupled meteorology and chemistry model, and it was used to simulate the formation processes that led
202 to high $PM_{2.5}$ loadings after the NCCPC. The WRF-Chem uses meteorological information, including
203 clouds, boundary layer, temperature, and winds; pollutant emissions; chemical transformation; transport
204 (e.g., advection, convection, and diffusion); photolysis and radiation; dry and wet deposition; and aerosol
205 interactions. A detailed description of the WRF-Chem model may be found in Li et al. (2011a; 2011b;
206 2012). A grid of 280×160 cells covering China with a horizontal resolution of 0.25° was used for the
207 simulation, which also included twenty-eight vertical layers from the Earth's surface up to 50 hPa. Seven
208 layers below 1 km were used to ensure a high vertical resolution near ground-level. The meteorological

209 initial and boundary conditions were retrieved from the National Centers for Environmental Prediction
 210 (NCEP) reanalysis dataset, and the chemical initial and boundary conditions were obtained from the 6 h
 211 output of the Model for Ozone and Related chemical Tracers (MOZART, Emmons et al., 2010).

212 In this study, the mean bias (MB), root mean square error (RMSE), and index of agreement (IOA) were
 213 used to evaluate the performance of WRF-Chem simulation. The IOA is representative of the relative
 214 difference between the predicted and measured values, and it varies from 0 to 1, with 1 indicating perfect
 215 performance of the model prediction. These parameters were calculated using the following equations (Li
 216 et al., 2011a):

$$217 \quad MB = \frac{1}{N} \sum_{i=1}^N (P_i - O_i) \quad (5)$$

$$218 \quad RMSE = \left[\frac{1}{N} \sum_{i=1}^N (P_i - O_i)^2 \right]^{\frac{1}{2}} \quad (6)$$

$$219 \quad IOA = 1 - \frac{\sum_{i=1}^N (P_i - O_i)^2}{\sum_{i=1}^N (|P_i - P_{ave}| + |O_i - O_{ave}|)^2} \quad (7)$$

220 where P_i and P_{ave} represent each predicted $PM_{2.5}$ mass concentration and the average value, respectively;
 221 O_i and O_{ave} are the observed $PM_{2.5}$ mass concentrations and the average value, respectively; and N is
 222 representative of the total number of predictions used for comparison.

223 2.3.4 Calculations of chemical b_{scat} and b_{abs}

224 To determine the contributions of individual $PM_{2.5}$ chemical species to particles' optical properties, b_{scat}
 225 and b_{abs} were reconstructed based on the major chemical composition of the $PM_{2.5}$ using the revised
 226 IMPROVE equations as follows (Pitchford et al., 2007):

$$227 \quad b_{scat} \approx 2.2 \times f_S(RH) \times [(NH_4)_2SO_4]_{small} + 4.8 \times f_L(RH) \times [(NH_4)_2SO_4]_{large} + 2.4 \times f_S(RH) \times \\ 228 \quad [NH_4NO_3]_{small} + 5.1 \times f_L(RH) \times [NH_4NO_3]_{large} + 2.8 \times [OM]_{small} + 6.1 \times [OM]_{large} + 1 \times \\ 229 \quad [Fine\ soil] \quad (8)$$

$$230 \quad [X]_{large} = \frac{[X]^2}{20 \mu g m^{-3}}, \text{ for } [X] < 20 \mu g m^{-3} \quad (9)$$

$$231 \quad [X]_{large} = [X], \text{ for } [X] \geq 20 \mu g m^{-3} \quad (10)$$

$$232 \quad [X]_{small} = [X] - [X]_{large} \quad (11)$$

233 where the mass concentrations of ammonium sulfate ($[(NH_4)_2SO_4]$) and ammonium nitrate ($[NH_4NO_3]$)
 234 were estimated by multiplying the concentrations of SO_4^{2-} and NO_3^- by factors of 1.375 and 1.29,

235 respectively (Tao et al., 2014); $f(\text{RH})$ is the water growth for the small (S) and large (L) modes of
236 $(\text{NH}_4)_2\text{SO}_4$ and NH_4NO_3 in $\text{PM}_{2.5}$; and $[\text{X}]$ represents the $\text{PM}_{2.5}$ composition as used in Eq. (8). This
237 analysis is based on the assumption that the particles were externally mixed. More detailed information
238 concerning the IMPROVE algorithms may be found in Pitchford et al. (2007).

239 A second assumption for this part of the study was that there was negligible absorption by brown carbon
240 in the visible region (Yang et al., 2009), and on this basis, the b_{abs} can be determined from the EC mass
241 concentration using linear regression (Eq. 12). As shown in Figure S2, the derived slope (a) and intercept
242 (b) for the regression model were $10.8 \text{ m}^2 \text{ g}^{-1}$ and -4.7 , respectively.

$$243 \quad b_{\text{abs}} = a \times [\text{EC}] + b \quad (12)$$

244 **2.3.5 DRF calculations**

245 The Tropospheric Ultraviolet and Visible (TUV) radiation model developed by the National Center for
246 Atmospheric Research was used to estimate the aerosol DRF for 180–730 nm at the Earth’s surface. A
247 detailed description of the model may be found in Madronich (1993). Aerosol DRF is mainly controlled
248 by the aerosol column burden and chemical composition, and important properties include the AOD,
249 aerosol absorption optical depth (AAOD), and single-scattering albedo ($\text{SSA} = (\text{AOD} - \text{AAOD}) / \text{AOD}$).
250 Based on an established relationship between the AODs measured with sunphotometer and the light
251 extinction coefficients ($b_{\text{ext}} = b_{\text{scat}} + b_{\text{abs}}$) observed with PAXs, an effective height can be retrieved which
252 makes it possible to convert the IMPROVE-based chemical b_{ext} values into the AODs or AAODs caused
253 by the $\text{PM}_{2.5}$. There are hygroscopic effects to consider, and therefore, the dry b_{ext} values measured here
254 were modified to the wet b_{ext} based on the water-growth function of particles described in Malm et al.
255 (2003). We note that the estimated chemical AODs were based on the assumption that the aerosols were
256 distributed homogeneously throughout an effective height.

257 Finally, the calculated chemical AOD and SSA for different $\text{PM}_{2.5}$ composition scenarios were used in
258 the TUV model to obtain shortwave radiative fluxes. Values for the surface albedo, another factor that
259 influences DRF, were obtained from the MOD43B3 product measured with the Moderate Resolution
260 Imaging Spectroradiometer (<https://modis-atmos.gsfc.nasa.gov/ALBEDO/index.html>). The solar
261 component in the TUV model was calculated using the δ -Eddington approximation, and the vertical
262 profile of b_{ext} used in the model was described in Palancar and Toselli (2004). The aerosol DRF is defined
263 as the difference between the net shortwave radiative flux with and without aerosol as follows:

$$264 \quad \text{DRF}_{\text{surface}} = \text{Flux (net)}_{\text{with aerosol, surface}} - \text{Flux (net)}_{\text{without aerosol, surface}} \quad (13)$$

265 **3 Results and discussion**

266 **3.1 Effectiveness of the control measures on reducing PM_{2.5}**

267 We divided the study period into two phases based on the dates that the pollution control measures were
268 put into effect (1) the NCCPC-control period from 12 to 24 October and (2) non-control period from 25
269 October to 4 November. Temporal variations in the PM_{2.5} mass concentrations and those of the major
270 aerosol components during these two phases are shown in Figure 2, and a statistical summary of those
271 data is presented in Table 1. During the NCCPC-control period, the PM_{2.5} mass concentrations remained
272 consistently low relative to the NAAQS II (75 $\mu\text{g m}^{-3}$), generally $< 75 \mu\text{g m}^{-3}$. In contrast, higher fine
273 particle loadings ($\text{PM}_{2.5} > 75 \mu\text{g m}^{-3}$) frequently were observed during the non-control period. On average,
274 the mass concentration of PM_{2.5} during the NCCPC-control period was $57.9 \pm 9.8 \mu\text{g m}^{-3}$, which is lower
275 by 31.2% compared with the non-control period ($84.1 \pm 38.8 \mu\text{g m}^{-3}$). Meanwhile, the PM_{2.5} mass
276 concentrations obtained from the China Environmental Monitoring Center also showed a decreasing trend
277 over most of the BTH region during the NCCPC-control period (see Figure S3). Compared with previous
278 events when pollution control measures were implemented in Beijing and surrounding areas, the percent
279 decrease in PM_{2.5} found for the present study falls within the lower limit of the 30–50% reduction for
280 Olympic Games (Wang et al., 2009; Li et al., 2013), but it is less than the range of 40–60% for the APEC
281 (Tang et al., 2015; Tao et al., 2016; J. Wang et al., 2017) or the range of 60–70% for the VDP (Han et al.,
282 2016; Liang et al., 2017; Lin et al., 2017).

283 As shown in Figure 2 (right panel), the chemical mass closure calculations for PM_{2.5} showed that on
284 average OM was the largest contributor (30.4%) to PM_{2.5} mass during the non-control period, followed
285 by NO₃⁻ (16.7%), fine soil (11.2%), and EC (7.6%). In contrast, OM (24.3%) and NO₃⁻ (22.9%) dominated
286 the PM_{2.5} mass during the NCCPC-control period, followed by SO₄²⁻ (9.8%), NH₄⁺ (9.1%), and EC (7.9%).
287 The OM mass concentration was decreased largely by 43.1% from 24.6 $\mu\text{g m}^{-3}$ during the non-control
288 period to 14.0 $\mu\text{g m}^{-3}$ during the NCCPC-control period. For secondary water-soluble inorganic ions, the
289 average mass concentrations of NO₃⁻ (13.4 $\mu\text{g m}^{-3}$ versus 16.9 $\mu\text{g m}^{-3}$) and NH₄⁺ (5.4 versus 6.8 $\mu\text{g m}^{-3}$)
290 were lower by 20.7% and 20.6% during the NCCPC-control period, respectively. However, SO₄²⁻
291 exhibited similar loadings during the NCCPC-control (5.8 $\mu\text{g m}^{-3}$) and non-control (5.3 $\mu\text{g m}^{-3}$) periods.
292 This is consistent with the small differences in SO₂ concentrations for the NCCPC-control (8.5 $\mu\text{g m}^{-3}$,
293 Figure S4) versus the non-control (12.4 $\mu\text{g m}^{-3}$, Figure S4) periods. Indeed, the low SO₂ concentrations
294 may not have provided sufficient gaseous precursor to form substantial amounts of sulfate. The loadings
295 of EC, Cl⁻, and fine soil were lower by 25.0, 44.8, and 40.8%, respectively, when the controls were in

296 place. The variations in reductions for specific aerosol components imply differences in the effectiveness
297 of the emission controls on the chemical species, but as discussed below, meteorological conditions
298 probably had an influence on the loadings, too.

299 As shown in Figure S4, both WSs (0.7 ± 0.3 versus $1.3 \pm 0.8 \text{ m s}^{-1}$) and MLHs (304.3 ± 60.6 versus 373.7
300 $\pm 217.9 \text{ m}$) were lower for the NCCPC-control period compared with the non-control period. This
301 indicates that horizontal and vertical dispersion were weaker during the NCCPC-control period than in
302 the non-control period. More to the point, this shows that one needs to consider the effects of WS and
303 MLH to fully evaluate the effectiveness of the pollution control measures. A simple and effective way to
304 do this is to compare the concentrations of air pollutants for the two periods when atmospheric conditions
305 were stable (Wang et al., 2015; Liang et al., 2017).

306 We first evaluated atmospheric stability based on relationships between $\text{PM}_{2.5}$ mass concentrations and
307 WS and MLH. As shown in Figure 3, the $\text{PM}_{2.5}$ mass concentrations exhibited a power function
308 relationship with WS ($r = -0.65$) and MLH ($r = 0.77$). The approach used to determine stable conditions
309 was to find the WS and MLH values that were less than the inflection points in the $\text{PM}_{2.5}$ loadings; that
310 is, where the slopes in the loadings changed from large to relatively small values. As there are no true
311 inflection points for the power functions, we used piecewise functions to represent them. As shown in
312 Figure 3, the intersections of two linear regressions can be used to represent the inflection points of the
313 influences of meteorological conditions on $\text{PM}_{2.5}$ mass. Using these criteria, days with $\text{WS} < 0.4 \text{ m s}^{-1}$
314 and $\text{MLH} < 274 \text{ m}$ were subjectively considered to have stable atmospheric conditions.

315 There were two days for the NCCPC-control period and three days for the non-control period that satisfied
316 the stability criteria. The surface charts (Figure S5) show that the weather conditions for those selected
317 stable atmosphere days during the NCCPC-control and non-control periods were mainly controlled by
318 uniform pressure fields and weak low-pressure systems, respectively, and those conditions led to weak or
319 calm surface winds. Due to the lower WS (0.2 versus 0.3 m s^{-1}) and MLH (213 versus 244 m) during the
320 NCCPC-control period relative to the non-control period, the horizontal and vertical dispersion for the
321 stable atmospheric days were slightly weaker during the NCCPC-control period. As shown in Table 1,
322 the percent differences for $\text{PM}_{2.5}$ (43.4%), NO_3^- (25.9%), OM (68.1%), EC (40.0%), and fine soil (58.7%)
323 were larger for the days with stable atmospheric conditions compared with those for all days. These results
324 are a further indication that the control measures were effective in reducing pollution, but meteorology
325 also influenced the aerosol pollution.

326 **3.2 Estimates of source contributions**

327 The mass concentrations of water-soluble inorganic ions (SO_4^{2-} , NO_3^- , NH_4^+ , K^+ , and Cl^-), carbonaceous
328 (OC and EC), and elements (Al, Si, Ca, Ti, Cr, Mn, Fe, Cu, Zn, As, Br, and Pb) were used as data inputs
329 for the PMF 5.0 model. Through comparisons between the PMF profiles and reference profiles from
330 previous studies, the presumptive sources for the aerosol were identified as (i) coal combustion, (ii)
331 traffic-related emissions, (iii) secondary source, (iv) biomass burning, (v) industrial processes, and (vi)
332 mineral dust. As shown in Figure S6, the PMF modelled $\text{PM}_{2.5}$ mass concentrations were strongly
333 correlated with the observed values ($r = 0.98$, slope = 0.94), and the model-calculated concentrations for
334 each chemical species exhibited good linearity and correlations with the measured values ($r = 0.68\text{--}0.99$)
335 (Table S1). These results show that the six identified sources were physically interpretable and accounted
336 for much of the variability in the data.

337 Figure 4 presents the source profiles and the average contribution of each source to $\text{PM}_{2.5}$ mass during
338 the NCCPC-control and non-control periods. The first source factor was identified as coal burning
339 emissions because it was enriched with As (38.8%), Pb (32.9%), and Fe (30.3%) and had moderate
340 loadings of Mn (26.2%), Zn (23.8%), Si (23.1%), and Ca (22.8%) (Figure 4a). Of these elements, As is a
341 well-known tracer for coal burning (Hsu et al., 2009; Y. Chen et al., 2017); Pb, Fe, Mn, and Zn (Xu et al.,
342 2012; Men et al., 2018) are enriched in particles generated by this source; and Ca and Si can be
343 components of coal fly ash (Pipal et al., 2011). There was no significant difference in $\text{PM}_{2.5}$ loadings
344 contributed by this source between the NCCPC-control ($8.5 \mu\text{g m}^{-3}$) and non-control ($7.8 \mu\text{g m}^{-3}$) periods.
345 This may be because coal burning is mainly used for domestic purposes, especially heating, and the
346 control measures did not include this sector. The contribution of coal burning to $\text{PM}_{2.5}$ mass in our
347 October/November study was lower than its contribution in the BTH region in winter ($\sim 20\text{--}60 \mu\text{g m}^{-3}$)
348 (Huang et al., 2017), and that can be explained by the increased domestic usage of coal for heating
349 activities during the colder winter season.

350 The second source factor was linked to traffic-related emissions, and it was characterized by strong
351 loadings of EC (42.1%) and Cu (40.7%) and moderate contributions of OC (29.1%), Zn (27.1%), and Br
352 (22.2%). Previous studies have indicated that carbonaceous aerosols are components of gasoline and
353 diesel engine exhaust (Cao et al., 2005), and therefore, EC and OC have been used as indicators for motor
354 vehicle emissions (Chalbot et al., 2013; Khan et al., 2016a), and Br, too, may be emitted from internal
355 combustion engines (Bukowiecki et al., 2005). Aerosol Cu and Zn are derived from other types of vehicle
356 emissions, including those associated with lubricant and oil, brake linings, metal brake wear, and tires

357 (Lin et al., 2015). Furthermore, the mass concentration of PM_{2.5} from this source was strongly correlated
358 ($r = 0.72$) with vehicle-related NO_x concentrations (Figure S7), which further suggests the validity of this
359 PMF-resolved source. Traffic-related emissions showed similar percent contributions to PM_{2.5} mass
360 during the NCCPC-control (14.8%) and non-control (15.4%) periods (Figure 4c), but the mass
361 concentration was 38% lower for the NCCPC-control period ($8.9 \mu\text{g m}^{-3}$) than the non-control period
362 ($14.4 \mu\text{g m}^{-3}$). This shows that the reduction in motor vehicle activity during the control period led to
363 better air quality.

364 The third source factor was a clear signal of secondary particle formation because it was dominated by
365 high loadings of SO₄²⁻ (45.4%), NO₃⁻ (43.4%), and NH₄⁺ (47.0%) (Zhang et al., 2013; Amil et al., 2016).
366 Thus, this factor was assigned to the secondary source. Moreover, moderate loadings of As (30.5%), Pb
367 (27.4%), Cr (31.4%), Cu (30.7%), and EC (30.8%) also were assigned to this factor, suggesting influences
368 from coal burning and vehicle exhaust emissions. Although the concentrations of gaseous precursors,
369 especially SO₂ and NO_x, were lower during the NCCPC-control period (Figure S4), the average mass
370 contribution of secondary PM_{2.5} was larger when the controls were in effect (22.5 versus $18.3 \mu\text{g m}^{-3}$);
371 indeed, this source was the largest contributing factor (37.3% of PM_{2.5} mass) during the NCCPC-control
372 period. We note that the higher RH (84%) during the NCCPC-control period compared with the non-
373 control period (69%) may have promoted the formation of the secondary inorganic aerosols through
374 aqueous reactions (Sun et al., 2014).

375 The fourth source factor, identified as emissions from biomass burning, was characterized by the high
376 loadings of K⁺ (59.5%) and moderate loadings of Cl⁻ (33.3%), OC (28.5%), NO₃⁻ (37.1%), SO₄²⁻ (21.1%),
377 and NH₄⁺ (39.6%). Soluble K⁺ is an established tracer for biomass burning (Zhang et al., 2013; Wang et
378 al., 2016b), and Cl⁻ and OC also are emitted during biomass burning (Tao et al., 2014; Huang et al., 2017).
379 Previous studies have shown that SO₂ and NO₂ can be converted into sulfate and nitrate on KCl particles
380 during the transport of biomass-burning emissions (Du et al., 2011). Therefore, the abundant NO₃⁻, SO₄²⁻,
381 and NH₄⁺ associated with this factor may be indicative of aged biomass-burning particles. As shown in
382 Figure 4c, biomass burning contributed substantially to PM_{2.5} mass during both the NCCPC (21.6%) and
383 non-control periods (27.3%). This is to be expected because Hebei Province is a major corn and wheat
384 producing area, and the residues of these crops commonly are used for residential cooking and heating or
385 burned in the fields (J. Chen et al., 2017). The mass concentrations of PM_{2.5} from this source were lower
386 during the NCCPC ($13.0 \mu\text{g m}^{-3}$) than in the non-control period ($25.7 \mu\text{g m}^{-3}$), and this indicates the
387 effectiveness of the control policy that forbade the open space biomass-burning during the NCCPC. As

388 the control measures did not include prohibitions on the household use of biofuels, substantial
389 contributions of biomass burning were still evident during the NCCPC-control period.

390 The fifth source factor was identified as emissions from industrial processes because it had high loadings
391 of Zn (41.3%), Br (38.0%), Pb (19.9%), As (19.2%), Cu (17.5%), and Mn (19.1%) (Q. Q. Wang et al.,
392 2017; Sammaritano et al., 2018). This source contributed $3.6 \mu\text{g m}^{-3}$ to $\text{PM}_{2.5}$ mass during the NCCPC-
393 control period, which was lower than the non-control period ($16.2 \mu\text{g m}^{-3}$) by 78%, and its percent
394 contribution to $\text{PM}_{2.5}$ mass also increased correspondingly from 6.0 to 17.2% after the controls were
395 removed. The results showed that restrictions on industrial activities during the NCCPC-control period
396 led to improvements in air quality. Iron and steel production are among the most important industries in
397 BTH region, and the iron and steel production there accounted for 28.8% of the total for China in 2016
398 (NBS, 2017). The sintering process in iron and steel industries produce large amounts of heavy metal
399 pollutants including Zn, Pb, and Mn (Duan and Tan, 2013). Hence, the iron and steel industries in the
400 BTH region were probable sources for these metals during the non-control period.

401 The sixth source factor was obviously mineral dust because it had high loadings of Al (55.9%), Si (55.7%),
402 Ca (52.6%), and Ti (36.7%) (Zhang et al., 2013; Tao et al., 2014; Kuang et al., 2015). This factor
403 contributed $3.8 \mu\text{g m}^{-3}$ (6.3% of $\text{PM}_{2.5}$ mass) during the NCCPC-control period and $11.5 \mu\text{g m}^{-3}$ (12.3%)
404 to $\text{PM}_{2.5}$ mass in the non-control period. Possible sources for the mineral dust include (i) natural dust,
405 which contains crustal Al, Si, and Ti (Milando et al., 2016), (ii) construction dust, which includes Ca (Liu
406 et al., 2017), and (iii) road dust, which is characterized by traffic-related species, such as Cu, Zn, Br, and
407 EC (Khan et al., 2016b; Zong et al., 2016). Here, the mineral dust factor did not contain any notable
408 contributions from the traffic-related species. Thus, this factor can be explained by the natural and
409 construction dusts. As shown in Figure S8, WS was positively correlated ($r = 0.75$) with the $\text{PM}_{2.5}$ mass
410 from mineral dust. To reduce the effects of wind speed on crustal dust resuspension, we compared the
411 days with low winds ($< 1 \text{ m s}^{-1}$) during the sampling periods, and only three sampling days were excluded
412 from the analysis. This comparison showed that the mass concentration of $\text{PM}_{2.5}$ from mineral dust was
413 60.0% lower in the NCCPC-control period ($3.8 \mu\text{g m}^{-3}$) compared with the non-control period ($9.5 \mu\text{g m}^{-3}$).
414 This was a strong indication that restrictions on construction activities during the NCCPC-period were
415 effective in reducing the mineral dust component of $\text{PM}_{2.5}$, but as noted above, this was not a large
416 component of the $\text{PM}_{2.5}$ mass.

417 3.3 Pollution episodes after the NCCPC-control period

418 As shown in Figure 2 (left panel), two pollution episodes occurred after the NCCPC-control period (PE1:
419 25–27 October and PE2: 31 October–1 November); the average $PM_{2.5}$ mass concentrations in PE1 and
420 PE2 were 117.5 and $124.5 \mu\text{g m}^{-3}$, respectively. For PE1, secondary source was the dominant contributor
421 to the fine particle population, accounting for 54.6% of $PM_{2.5}$ mass (Figure 5a), and the secondary species
422 that showed the largest contribution to $PM_{2.5}$ mass was NO_3^- (26.8%) (Figure 5b). The mass concentration
423 of NO_3^- increased from $< 10 \mu\text{g m}^{-3}$ before PE1 to $> 25 \mu\text{g m}^{-3}$ during the episode (Figure 2). Molar ratios
424 of NO_3^- to NO_2 ($\text{NOR} = n\text{-NO}_3^- / (n\text{-NO}_2 + n\text{-NO}_3^-)$) were calculated to investigate nitrogen partitioning
425 between the particulate and gas phases (Zhang et al., 2011). As shown in Figure 6a, the mass concentration
426 of $PM_{2.5}$ increased with NOR ($r = 0.65$) throughout the entire campaign, which indicates that nitrate
427 formation was involved in the high $PM_{2.5}$ loadings. The NORs ranged from 0.32 to 0.71 during the PE1,
428 and those values were significantly different (t -test, $p < 0.01$) from the ratios before (0.23–0.29) or after
429 PE1 (0.03–0.10), thus reflecting stronger nitrate formation during the pollution period. Furthermore, NOR
430 exhibited an exponential increase with RH ($r = 0.80$, Figure 6b), and the higher RHs (91–93%) during the
431 PE1 may have led to greater aqueous nitrate production relative to the periods before (80–86%) or after
432 (33–57%) the first pollution episode.

433 The second largest contributor to $PM_{2.5}$ mass during PE1 was OM, which accounted for 22.9% of the fine
434 aerosol mass. A widely used EC-tracer method (Lim and Turpin, 2002) was used to estimate the primary
435 and secondary OA (POA and SOA). For this, the lowest 10% percentile of the measured OC/EC ratios
436 was used as a measure of the primary OC/EC ratio (Zheng et al., 2015). The estimated mass
437 concentrations of POA and SOA were 17.2 and $9.7 \mu\text{g m}^{-3}$ during the PE1, which amounted to 63.9 and
438 36.1% of the OM mass, respectively.

439 Photochemical oxidation and aqueous reactions are two of the major mechanisms that lead to the
440 formation SOA (Hallquist et al., 2009), and we evaluated the roles of these chemical reactions by
441 investigating trends in the EC-scaled concentrations of SOA (SOA/EC). We note that normalizing the
442 data in this way eliminates the impacts of different dilution/mixing conditions on the SOA loadings
443 (Zheng et al., 2015). As shown in Figure 6c, the SOA/EC ratios increased ($r = 0.65$) with Ox ($\text{NO}_2 + \text{O}_3$),
444 which is a proxy for atmospheric aging caused by photochemical reactions (Canonaco et al., 2015), and
445 the EC-scaled concentrations showed a weaker correlation with RH ($r = -0.32$) (Figure 6d). These results
446 indicate that photochemical reactions rather than aqueous phase oxidation were the major pathways for

447 SOA formation. Thus, the small contribution of SOA to PM_{2.5} during the PE1 may have been due to low
448 photochemical activity during that episode.

449 In contrast to the first pollution episode, OM (31.8%) was the most abundant PM_{2.5} species during PE2,
450 and that was followed by NO₃⁻ (19.2%) (Figure 5b). The mass concentration of K⁺ increased substantially,
451 from 0.1 μg m⁻³ before PE2 to 1.7 μg m⁻³ during the event, indicating a strengthening influence of
452 biomass-burning emissions. Indeed, the results of PMF showed that biomass burning was the largest
453 contributor to PM_{2.5} mass during the PE2, accounting for 36.0% of the total (Figure 5a). Furthermore, the
454 72-h back trajectories showed that air masses sampled during the PE2 either originated from or passed
455 over areas with fires in Inner Mongolia and Shanxi Province (see Figure 7), and this can explain the
456 apparent impacts from biomass burning emission. Moreover, SOA contributed an estimated 47.7% of the
457 OM mass, and that is a strong indication that secondary organics were a major component of the pollution.
458 The mass concentration of SOA was 19.0 μg m⁻³ during the PE2, and that was higher than in 9.7 μg m⁻³
459 during the PE1. As the oxidizing conditions—as indicated by Ox—were similar for both pollution
460 episodes (78.0 μg m⁻³ in PE1 versus 86.7 μg m⁻³ in PE2) (Figure S4), the larger SOA during the PE2 can
461 best be explained by SOA that formed from gaseous biomass-burning emissions during transport.

462 **3.4 Meteorological considerations**

463 Previous studies have shown that meteorological conditions play an important role in the accumulation
464 of pollution in the BTH region (Bei et al., 2017). Surface weather charts (Figure 8) were used to analyze
465 the synoptic conditions during the two pollution episodes, and the WRF-Chem model was applied to
466 simulate the formation of PM_{2.5} (Figure 9). As shown in Figure S9, the predicted PM_{2.5} and its major
467 chemical components exhibited trends roughly similar to the observed values. The calculated MB and
468 RMSE for PM_{2.5} were -6.8 and 32.8 μg m⁻³, and the IOA was 0.75, indicating that the formation of PM_{2.5}
469 during the two pollution episodes was reasonably well captured by the WRF-Chem model even though
470 the predicted average PM_{2.5} mass concentration was lower than the observed value. The most probable
471 reason for this is that uncertainties associated with the complex meteorological fields can affect the
472 transport, diffusion, and removal of air pollutants in the atmosphere (Bei et al., 2012). Additionally,
473 discrepancies in the emission inventories for PM_{2.5} for different years may have contributed to the
474 differences in modelled versus measured values.

475 On 22 October, that is, before PE1, a weak cold high-pressure system in Siberia moved southward (Figure
476 8), and the BTH region was under the influence of a cold high-pressure system; conditions such as those
477 tend to keep pollutants at low levels. After the passage of the low-pressure system, the BTH region was

478 under the control of a weak high-pressure system from 24 to 25 October, and that led to a convergence of
479 southerly airflow in the BTH region. Those meteorological conditions were favourable for the gradual
480 accumulation of pollutants (Figure 9). For example, as shown in Figure S4, the NO_x concentrations
481 increased from 71.6 μg m⁻³ on 22 October to 147.6 μg m⁻³ on 25 October, and that increase provided a
482 supply of gaseous precursors that can explain the observed large loadings of aerosol nitrate.

483 On 28 October, the first day of PE1, cold air piled up in the BTH region, and the high-pressure system
484 gradually strengthened. The weather in the BTH region at that time was characterized by cloudiness, high
485 RH, and low surface WSs. Those conditions promoted the accumulation of pollutants (Figure 9), and the
486 WRF-Chem simulation indicated that the BTH region contributed 73.6% of PM_{2.5} mass during PE1. On
487 29 October, the cold high-pressure system moved towards the south, and northerly winds increased. Those
488 meteorological conditions presumably led to a dilution of the air pollutants, and as a result, lower PM_{2.5}
489 loadings were observed in the BTH region (Figure 9).

490 From 31 October–1 November (PE2), the BTH region was again dominated by a weak high-pressure
491 system, and a convergence of northerly airflow was caused by the high-pressure system and a trailing
492 low-pressure front. Local pollutants from the BTH region would have accumulated under those conditions,
493 but as discussed above, the loadings of PM_{2.5} also can be affected by the long-range transport processes.
494 Indeed, the WRF-Chem simulation indicated that the BTH region contributed 46.9% to PM_{2.5} mass,
495 similar to the import of fine particles from other regions (53.1%). After 2 November, the cold high-
496 pressure system began to move southward, the winds strengthened, and the air quality gradually improved.

497 **3.5 Impacts of PM_{2.5} emission reduction on aerosol radiative effects**

498 The aerosol DRF refers to the change in the energy balance caused by the scattering and absorption of
499 radiant energy by aerosols. As shown in Figure S10, the reconstructed chemical b_{scat} correlated strongly
500 ($r = 0.91$) with the observed b_{scat} values; the slope of the linear regression was 0.90. This result indicates
501 that the IMPROVE-based method provided a good estimation of the chemical b_{scat} ; nonetheless, it is likely
502 that more locally-measured mass scattering efficiencies for each chemical species could reduce the
503 underestimates of measured values. Moreover, a significant ($p < 0.01$) relationship between the measured
504 b_{abs} and EC mass (Figure S2) validates the use of EC mass loadings in Eq. 12 to estimate the chemical
505 b_{abs} . The contributions of each measured PM_{2.5} component to the chemical b_{ext} were calculated based on
506 Eq. 8, and on average, OM was the largest contributor (43.5%) to the chemical b_{ext} during the non-control
507 period (Figure 10a), followed by NH₄NO₃ (32.4%), EC (14.3%), (NH₄)₂SO₄ (7.6%), and fine soil (2.2%).
508 In contrast, during the NCCPC-control period, NH₄NO₃ was the largest contributor to the chemical b_{ext} ,

509 amounting to 36.7% of b_{ext} , and it was followed by OM (33.3%), EC (16.2%), $(\text{NH}_4)_2\text{SO}_4$ (11.9%), and
510 fine soil (1.9%). The contributions of the various $\text{PM}_{2.5}$ components to b_{ext} were different compared with
511 previous studies of the pollution controls for the Olympics and APEC. For example, Li et al. (2013)
512 reported that $(\text{NH}_4)_2\text{SO}_4$ (41%) had the largest contribution to b_{ext} during the Olympics, followed by
513 NH_4NO_3 (23%), OM (17%), and EC (9%); Zhou et al. (2017) found that OM (49%) was the largest
514 contributor to b_{ext} during the APEC summit, followed by NH_4NO_3 (19%), $(\text{NH}_4)_2\text{SO}_4$ (13%), and EC
515 (12%). These differences may be attributed to variable efficiencies of the controls for the specific fine
516 particle species and to variations in RH among studies, the latter of which can influence sulfate and nitrate
517 formation.

518 As shown in Figure S11, the AODs measured with a sunphotometer were well correlated with the b_{ext}
519 under ambient conditions; the slope (effective height) of the regression was 708 m and $r = 0.78$. Based on
520 the average effective height, the estimated chemical AOD ($\text{AOD} = 708 \times b_{\text{ext}} \times 10^{-6}$) and SSA contributed
521 by each major component in $\text{PM}_{2.5}$ were entered into the TUV model to calculate the DRF at the Earth's
522 surface. The estimated average DRF ranged from -33.2 to -3.4 W m^{-2} , with an arithmetic mean \pm standard
523 deviation of $-16.5 \pm 6.7 \text{ W m}^{-2}$ for the campaign. The average DRF for our study is similar to the -13.7
524 W m^{-2} calculated for photosynthetically active radiation at Xianghe, China in autumn using the Santa
525 Barbara DISORT Atmospheric Radiative Transfer model (SBDART) (Xia et al., 2007a). Further
526 comparisons with previous estimates of DRFs in China at ultraviolet and visible wavelengths show that
527 the average value from our study is similar to that at the rural site of Taihu (-17.8 W m^{-2} , Xia et al., 2007b),
528 but it was less negative than at the suburban or urban sites of Linan (-73.5 W m^{-2} , Xu et al., 2003), Nanjing
529 (-39.4 W m^{-2} , Zhuang et al., 2014), or Xi'an (-100.5 W m^{-2} , Wang et al., 2016b). The more negative DRF
530 values correspond with high aerosol loadings during those studies.

531 The estimated average DRF during the NCCPC-control period was $-14.0 \pm 3.0 \text{ W m}^{-2}$, which was less
532 negative than the value during the non-control period ($-19.3 \pm 8.6 \text{ W m}^{-2}$) (Figure 10b), and this is
533 consistent with lower $\text{PM}_{2.5}$ mass loadings during the NCCPC-control period. Even though the DRF
534 values were as high as -24.7 and -28.2 W m^{-2} during PE1 and PE2, respectively, the percent reduction in
535 DRF during the NCCPC-control period versus the non-control period (26.3%) was smaller than the value
536 during the APEC-control study (61.3%, Zhou et al., 2017). Figure 10b also indicates that EC was
537 responsible for the largest (most negative) DRF effects at the surface during the non-control period: the
538 EC DRF value of -13.4 W m^{-2} was followed by OM (-3.0 W m^{-2}), NH_4NO_3 (-2.2 W m^{-2}), $(\text{NH}_4)_2\text{SO}_4$ (-
539 0.5 W m^{-2}), and fine soil (-0.15 W m^{-2}). The high EC DRF may have been due in part to EC particles

internally mixed with other materials because mixing can amplify light absorption and thereby increase DRF. The lower aerosol loadings during the NCCPC-control period can explain why the DRF values for EC, NH_4NO_3 , OM, and fine soil in the uncontrolled period were smaller in magnitude -10.1, -1.7, -1.6, and -0.09 W m^{-2} , respectively, than in the non-control period; these were equivalent to decreases of 24.6, 22.7, 46.7, and 40.0%. These results suggest that the short-term mitigation measures implemented during the NCCPC reduced the cooling effects of $\text{PM}_{2.5}$ at the surface in Beijing.

4 Conclusions

We investigated the effects of pollution controls put in place during the 19th NCCPC on the chemical composition of $\text{PM}_{2.5}$ and aerosol radiative effects at the Earth's surface. The average mass concentration of $\text{PM}_{2.5}$ during the NCCPC-control period was $57.9 \pm 9.8 \mu\text{g m}^{-3}$, which was 31.2% lower relative to the non-control period ($84.1 \pm 38.8 \mu\text{g m}^{-3}$). The major chemical species, that is, OM, NO_3^- , NH_4^+ , EC, and fine soil were lower by 43.1, 20.7, 20.6, 25.0, and 40.8% during the NCCPC-control period, respectively compared with samples taken after the controls were removed. Comparisons for only those days with stable meteorological conditions showed that the control versus non-control differences in $\text{PM}_{2.5}$ (43.4%), NO_3^- (25.9%), OM (68.1%), EC (40.0%), and fine soil (58.7%) were larger compared with those for all days. Overall, these results indicate that control measures were effective in reducing fine particle pollution. Results of a PMF receptor model showed that biomass burning (27.3%) was the largest contributor to $\text{PM}_{2.5}$ mass during the non-control period, followed by secondary source (19.5%), industrial processes (17.2%), traffic-related emissions (15.4%), mineral dust (12.3%), and coal burning (8.3%). In contrast, secondary source (37.3%) was the largest contributor to $\text{PM}_{2.5}$ mass during the NCCPC-control period, followed by biomass burning (21.6%), traffic-related emissions (14.8%), coal burning (14.1%), mineral dust (6.3%), and industrial processes (6.0%). The mass concentrations of $\text{PM}_{2.5}$ contributed by traffic-related emissions, biomass burning, industrial processes, and mineral dust all were lower during the NCCPC-control period compared with the non-control period. However, there was no significant difference in $\text{PM}_{2.5}$ mass from coal burning between these two periods, and a larger $\text{PM}_{2.5}$ mass concentration of secondary source was found for the NCCPC-control period.

There were two pollution episodes (PE1: 25–27 October and PE2: 31 October–1 November) that occurred after the NCCPC, and the average $\text{PM}_{2.5}$ mass concentrations during those events ($117.5 \mu\text{g m}^{-3}$ for PE1 and $124.5 \mu\text{g m}^{-3}$ for PE2) were more than double those when the controls were in place. For PE1, secondary source was the most important source for fine particles, accounting for 54.6% of $\text{PM}_{2.5}$ mass.

570 Aerosol NO_3^- showed the largest contribution to $\text{PM}_{2.5}$ mass (26.8%), and the high RH during PE1 likely
571 promoted aqueous reactions involving nitrate. In contrast, OM (31.8%) was the most abundant species in
572 $\text{PM}_{2.5}$ during the PE2, and the PMF indicated that biomass burning was the largest source, accounting for
573 36.0% of the $\text{PM}_{2.5}$ mass. The WRF-Chem simulation showed that the BTH region contributed 73.6%
574 and 46.9% of $\text{PM}_{2.5}$ mass during the PE1 and PE2, respectively.

575 Calculations based on methods developed for the IMPROVE program indicated that OM was the largest
576 contributor (43.5%) to the chemical b_{ext} during the non-control period, followed by NH_4NO_3 (32.4%), EC
577 (14.3%), $(\text{NH}_4)_2\text{SO}_4$ (7.6%), and fine soil (2.2%). During the NCCPC-control period, NH_4NO_3 accounted
578 for 36.7% of b_{ext} , and that was followed by OM (33.3%), EC (16.2%), $(\text{NH}_4)_2\text{SO}_4$ (11.9%), and fine soil
579 (1.9%). The TUV model showed that the estimated average DRF ($-14.0 \pm 3.0 \text{ W m}^{-2}$) at the surface during
580 the NCCPC-control period was 27.5% less negative than in the non-control period ($-19.3 \pm 8.6 \text{ W m}^{-2}$),
581 and this is consistent with the lower $\text{PM}_{2.5}$ loadings during the NCCPC-control period. Furthermore, EC
582 had the largest (most negative) influence on DRF at the surface during the non-control period; the EC
583 DRF value of -13.4 W m^{-2} was followed by OM (-3.0 W m^{-2}), NH_4NO_3 (-2.2 W m^{-2}), $(\text{NH}_4)_2\text{SO}_4$ (-0.5 W
584 m^{-2}), and fine soil (-0.15 W m^{-2}). The DRF values caused by EC, NH_4NO_3 , OM, and fine soil when the
585 controls were in place were lower by -10.1, -1.7, -1.6, and -0.09 W m^{-2} , respectively, compared with the
586 non-control period, and the corresponding percent reductions were 24.6, 22.7, 46.7, and 40.0%. The
587 results suggest that the short-term mitigation measures during the NCCPC-control period were effective
588 in reducing fine particle pollution and those actions also had radiative effects sufficient to affect surface
589 temperature.

590 **Author contribution**

591 QW and JC designed the research. QW, SL, WD, YW, JT, YZ, and MW carried out the measurements.
592 QW and NL performed the analysis, and QW wrote the paper. All the authors commented on the paper.

593

594 **Acknowledgments**

595 This work was supported by the National Research Program for Key Issues in Air Pollution Control
596 (DQGG0105) and the National Natural Science Foundation of China (41503118 and 41661144020). The
597 authors are grateful to the staff from Xianghe Atmospheric Observatory for their assistance with field
598 sampling.

- Amil, N., Latif, M. T., Khan, M. F., and Mohamad, M.: Seasonal variability of PM_{2.5} composition and sources in the Klang Valley urban-industrial environment, *Atmos. Chem. Phys.*, 16, 5357–5381, <https://doi.org/10.5194/acp-16-5357-2016>, 2016.
- Bei, N., Li, G., and Molina, L. T.: Uncertainties in SOA simulations due to meteorological uncertainties in Mexico City during MILAGRO-2006 field campaign, *Atmos. Chem. Phys.*, 12, 11295–11308, <https://doi.org/10.5194/acp-16-5357-2016>, 2012.
- Bei, N., Wu, J., Elser, M., Feng, T., Cao, J., El-Haddad, I., Li, X., Huang, R., Li, Z., Long, X., Xing, L., Zhao, S., Tie, X., Prévôt, A. S. H., and Li, G.: Impacts of meteorological uncertainties on the haze formation in Beijing–Tianjin–Hebei (BTH) during wintertime: a case study, *Atmos. Chem. Phys.*, 17, 14579–14591, <https://doi.org/10.5194/acp-17-14579-2017>, 2017.
- Bukowiecki, N., Hill, M., Gehrig, R., Zwicky, C. N., Lienemann, P., Hegedüs, F., Falkenberg, G., Weingartner, E., and Baltensperger, U.: Trace metals in ambient air: hourly size-segregated mass concentrations determined by synchrotron-XRF, *Environ. Sci. Technol.*, 39, 5754–5762, [doi:10.1021/es048089m](https://doi.org/10.1021/es048089m), 2005.
- Canonaco, F., Slowik, J. G., Baltensperger, U., and Prévôt, A. S. H.: Seasonal differences in oxygenated organic aerosol composition: implications for emissions sources and factor analysis, *Atmos. Chem. Phys.*, 15, 6993–7002, <https://doi.org/10.5194/acp-15-6993-2015>, 2015.
- Cao, J. J., Wang, Q. Y., Chow, J. C., Watson, J. G., Tie, X. X., Shen, Z. X., Wang, P., and An, Z. S.: Impacts of aerosol compositions on visibility impairment in Xi'an, China, *Atmos. Environ.*, 59, 559–566, <https://doi.org/10.1016/j.atmosenv.2012.05.036>, 2012.
- Cao, J. J., Lee, S. C., Ho, K. F., Zhang, X. Y., Zou, S. C., Fung, K., Chow, J. C., and Watson, J. G.: Characteristics of carbonaceous aerosol in Pearl River Delta Region, China during 2001 winter period, *Atmos. Environ.*, 37, 1451–1460, [https://doi.org/10.1016/S1352-2310\(02\)01002-6](https://doi.org/10.1016/S1352-2310(02)01002-6), 2003.
- Cao, J. J., Wu, F., Chow, J. C., Lee, S. C., Li, Y., Chen, S. W., An, Z. S., Fung, K. K., Watson, J. G., Zhu, C. S., and Liu, S. X.: Characterization and source apportionment of atmospheric organic and elemental carbon during fall and winter of 2003 in Xi'an, China, *Atmos. Chem. Phys.*, 5, 3127–3137, <https://doi.org/10.5194/acp-5-3127-2005>, 2005.
- Chalbot, M. C., McElroy, B., and Kavouras, I. G.: Sources, trends and regional impacts of fine particulate matter in southern Mississippi valley: significance of emissions from sources in the Gulf of Mexico coast, *Atmos. Chem. Phys.*, 13, 3721–3732, <https://doi.org/10.5194/acp-13-3721-2013>, 2013.
- Chen, J., Li, C., Ristovski, Z., Milic, A., Gu, Y., Islam, M. S., Wang, S., Hao, J., Zhang, H., He, C., Guo, H., Fu, H., Miljevic, B., Morawska, L., Thai, P., Lam, Y. F., Pereira, G., Ding, A., Huang, X., and Dumka, U. C.: A review of biomass burning: Emissions and impacts on air quality, health and climate in China, *Sci. Total Environ.*, 579, 1000–1034, <https://doi.org/10.1016/j.scitotenv.2016.11.025>, 2017.
- Chen, Y., Xie, S. D., Luo, B., and Zhai, C. Z.: Particulate pollution in urban Chongqing of southwest China: Historical trends of variation, chemical characteristics and source apportionment, *Sci. Total Environ.*, 584–585, 523–534, <https://doi.org/10.1016/j.scitotenv.2017.01.060>, 2017.
- Cheung, K., Daher, N., Shafer, M. M., Ning, Z., Schauer, J. J., and Sioutas, C.: Diurnal trends in coarse particulate matter composition in the Los Angeles Basin, *J. Environ. Monit.*, 13, 3277–3287, [doi:10.1039/c1em10296f](https://doi.org/10.1039/c1em10296f), 2011.
- Chow, J. C., Watson, J. G., Chen, L. W. A., Chang, M. C. O., Robinson, N. F., Trimble, D., and Kohl, S.: The IMPROVE_A Temperature Protocol for Thermal/Optical Carbon Analysis: Maintaining Consistency with a Long-Term Database, *J. Air Waste Manage. Assoc.*, 57, 1014–1023, <https://doi.org/10.3155/1047-3289.57.9.1014>, 2007.

645 Draxler, R. R. and Rolph, G. D.: HYSPLIT (HYbrid Single-Particle Lagrangian Integrated Trajectory),
646 Silver Spring, MD, Model access via NOAA ARL READY Website:
647 <http://www.arl.noaa.gov/ready/hysplit4.html>NOAA AirResourcesLaboratory (last access: February
648 2018), 2003

649 Du, H., Kong, L., Cheng, T., Chen, J., Du, J., Li, L., Xia, X., Leng, C., and Huang, G.: Insights into
650 summertime haze pollution events over Shanghai based on online water-soluble ionic composition
651 of aerosols, *Atmos. Environ.*, 45, 5131–5137, <https://doi.org/10.1016/j.atmosenv.2011.06.027>, 2011.

652 Duan, J., and Tan, J.: Atmospheric heavy metals and Arsenic in China: Situation, sources and control
653 policies, *Atmos. Environ.*, 74, 93–101, <https://doi.org/10.1016/j.atmosenv.2013.03.031>, 2013.

654 Elser, M., Huang, R. J., Wolf, R., Slowik, J. G., Wang, Q. Y., Canonaco, F., Li, G., Bozzetti, C.,
655 Daellenbach, K. R., Huang, Y., Zhang, R., Li, Z., Cao, J., Baltensperger, U., El-Haddad, I., and
656 Prévôt, A. S. H.: New insights into PM_{2.5} chemical composition and sources in two major cities in
657 China during extreme haze events using aerosol mass spectrometry, *Atmos. Chem. Phys.*, 16, 3207–
658 3225, <https://doi.org/10.5194/acp-16-3207-2016>, 2016.

659 Emmons, L. K., Walters, S., Hess, P. G., Lamarque, J. F., Pfister, G. G., Fillmore, D., Granier, C.,
660 Guenther, A., Kinnison, D., Laepple, T., Orlando, J., Tie, X., Tyndall, G., Wiedinmyer, C.,
661 Baughcum, S. L., and Kloster, S.: Description and evaluation of the Model for Ozone and Related
662 chemical Tracers, version 4 (MOZART-4), *Geosci. Model Dev.*, 3, 43–67,
663 <https://doi.org/10.5194/gmd-3-43-2010>, 2010.

664 Feng, S. L., Gao, D., Liao, F., Zhou, F. R., and Wang, X. M.: The health effects of ambient PM_{2.5} and
665 potential mechanisms, *Ecotox. Environ. Safe.*, 128, 67–74,
666 <https://doi.org/10.1016/j.ecoenv.2016.01.030>, 2016.

667 Gao, Y., Liu, X., Zhao, C., and Zhang, M.: Emission controls versus meteorological conditions in
668 determining aerosol concentrations in Beijing during the 2008 Olympic Games, *Atmos. Chem. Phys.*,
669 11, 12437–12451, <https://doi.org/10.5194/acp-11-12437-2011>, 2011.

670 Guo, S., Hu, M., Guo, Q., Zhang, X., Schauer, J. J., and Zhang, R.: Quantitative evaluation of emission
671 controls on primary and secondary organic aerosol sources during Beijing 2008 Olympics, *Atmos.*
672 *Chem. Phys.*, 13, 8303–8314, <https://doi.org/10.5194/acp-13-8303-2013>, 2013.

673 Hallquist, M., Wenger, J. C., Baltensperger, U., Rudich, Y., Simpson, D., Claeys, M., Dommen, J.,
674 Donahue, N. M., George, C., Goldstein, A. H., Hamilton, J. F., Herrmann, H., Hoffmann, T., Iinuma,
675 Y., Jang, M., Jenkin, M. E., Jimenez, J. L., Kiendler-Scharr, A., Maenhaut, W., McFiggans, G.,
676 Mentel, T. F., Monod, A., Prévôt, A. S. H., Seinfeld, J. H., Surratt, J. D., Szmigielski, R., and Wildt,
677 J.: The formation, properties and impact of secondary organic aerosol: current and emerging issues,
678 *Atmos. Chem. Phys.*, 9, 5155–5236, <https://doi.org/10.5194/acp-9-5155-2009>, 2009.

679 Han, X., Guo, Q., Liu, C., Strauss, H., Yang, J., Hu, J., Wei, R., Tian, L., Kong, J., and Peters, M.: Effect
680 of the pollution control measures on PM_{2.5} during the 2015 China Victory Day Parade: Implication
681 from water-soluble ions and sulfur isotope, *Environ. Pollut.*, 218, 230–241,
682 <https://doi.org/10.1016/j.envpol.2016.06.038>, 2016.

683 Hsu, S.-C., Liu, S. C., Huang, Y.-T., Chou, C. C. K., Lung, S. C. C., Liu, T.-H., Tu, J.-Y., and Tsai, F.:
684 Long-range southeastward transport of Asian biomass pollution: Signature detected by aerosol
685 potassium in Northern Taiwan, *J. Geophys. Res.-Atmos.*, 114, D14301, doi:10.1029/2009JD011725,
686 2009.

687 Huang, X., Liu, Z., Liu, J., Hu, B., Wen, T., Tang, G., Zhang, J., Wu, F., Ji, D., Wang, L., and Wang, Y.:
688 Chemical characterization and source identification of PM_{2.5} at multiple sites in the Beijing-Tianjin-
689 Hebei region, China, *Atmos. Chem. Phys.*, 17, 12941–12962, [https://doi.org/10.5194/acp-17-12941-](https://doi.org/10.5194/acp-17-12941-2017)
690 2017, 2017.

- 691 Khan, M. F., Sulong, N. A., Latif, M. T., Nadzir, M. S. M., Amil, N., Hussain, D. F. M., Lee, V., Hosaini,
692 P. N., Shaharom, S., Yusoff, N. A. Y. M., Hoque, H. M. S., Chung, J. X., Sahani, M., Mohd Tahir,
693 N., Juneng, L., Maulud, K. N. A., Abdullah, S. M. S., Fujii, Y., Tohno, S., and Mizohata, A.:
694 Comprehensive assessment of PM_{2.5} physicochemical properties during the Southeast Asia dry
695 season (southwest monsoon), *J. Geophys. Res.-Atmos.*, 121, 14589–14611,
696 doi:10.1002/2016JD025894, 2016a.
- 697 Khan, M. F., Latif, M. T., Saw, W. H., Amil, N., Nadzir, M. S. M., Sahani, M., Tahir, N. M., and Chung,
698 J. X.: Fine particulate matter in the tropical environment: monsoonal effects, source apportionment,
699 and health risk assessment, *Atmos. Chem. Phys.*, 16, 597–617, [https://doi.org/10.5194/acp-16-597-](https://doi.org/10.5194/acp-16-597-2016)
700 2016, 2016b.
- 701 Kuang, B. Y., Lin, P., Huang, X. H. H., and Yu, J. Z.: Sources of humic-like substances in the Pearl River
702 Delta, China: positive matrix factorization analysis of PM_{2.5} major components and source markers,
703 *Atmos. Chem. Phys.*, 15, 1995–2008, <https://doi.org/10.5194/acp-15-1995-2015>, 2015.
- 704 Lecoecur, E., Seigneur, C., Page, C., and Terray, L.: A statistical method to estimate PM_{2.5} concentrations
705 from meteorology and its application to the effect of climate change, *J. Geophys. Res.-Atmos.*, 119,
706 3537–3585, doi:10.1002/2013JD021172, 2014.
- 707 Li, G., Bei, N., Tie, X., and Molina, L. T.: Aerosol effects on the photochemistry in Mexico City during
708 MCMA-2006/MILAGRO campaign, *Atmos. Chem. Phys.*, 11, 5169–5182,
709 <https://doi.org/10.5194/acp-11-5169-2011>, 2011a.
- 710 Li, G., Zavala, M., Lei, W., Tsimpidi, A. P., Karydis, V. A., Pandis, S. N., Canagaratna, M. R., and Molina,
711 L. T.: Simulations of organic aerosol concentrations in Mexico City using the WRF-CHEM model
712 during the MCMA-2006/MILAGRO campaign, *Atmos. Chem. Phys.*, 11, 3789–3809,
713 <https://doi.org/10.5194/acp-11-3789-2011>, 2011b.
- 714 Li, G., Lei, W., Bei, N., and Molina, L. T.: Contribution of garbage burning to chloride and PM_{2.5} in
715 Mexico City, *Atmos. Chem. Phys.*, 12, 8751–8761, <https://doi.org/10.5194/acp-12-8751-2012>, 2012.
- 716 Li, J., Xie, S. D., Zeng, L. M., Li, L. Y., Li, Y. Q., and Wu, R. R.: Characterization of ambient volatile
717 organic compounds and their sources in Beijing, before, during, and after Asia-Pacific Economic
718 Cooperation China 2014, *Atmos. Chem. Phys.*, 15, 7945–7959, [https://doi.org/10.5194/acp-15-](https://doi.org/10.5194/acp-15-7945-2015)
719 7945-2015, 2015.
- 720 Li, J., and Han, Z.: A modeling study of severe winter haze events in Beijing and its neighboring regions,
721 *Atmos. Res.*, 170, 87–97, <https://doi.org/10.1016/j.atmosres.2015.11.009>, 2016.
- 722 Li, X., He, K., Li, C., Yang, F., Zhao, Q., Ma, Y., Cheng, Y., Ouyang, W., and Chen, G.: PM_{2.5} mass,
723 chemical composition, and light extinction before and during the 2008 Beijing Olympics, *J. Geophys.*
724 *Res.-Atmos.*, 118, 12158–12167, doi:10.1002/2013JD020106, 2013.
- 725 Liang, P., Zhu, T., Fang, Y., Li, Y., Han, Y., Wu, Y., Hu, M., and Wang, J.: The role of meteorological
726 conditions and pollution control strategies in reducing air pollution in Beijing during APEC 2014
727 and Victory Parade 2015, *Atmos. Chem. Phys.*, 17, 13921–13940, [https://doi.org/10.5194/acp-17-](https://doi.org/10.5194/acp-17-13921-2017)
728 13921-2017, 2017.
- 729 Lim, H.-J., and Turpin, B. J.: Origins of primary and secondary organic aerosol in Atlanta: Results of
730 time-resolved measurements during the Atlanta Supersite Experiment, *Environ. Sci. Technol.*, 36,
731 4489–4496, doi:10.1021/es0206487, 2002.
- 732 Lin, H., Liu, T., Fang, F., Xiao, J., Zeng, W., Li, X., Guo, L., Tian, L., Schootman, M., Stamatakis, K. A.,
733 Qian, Z., and Ma, W.: Mortality benefits of vigorous air quality improvement interventions during
734 the periods of APEC Blue and Parade Blue in Beijing, China, *Environ. Pollut.*, 220, 222–227,
735 <https://doi.org/10.1016/j.envpol.2016.09.041>, 2017.
- 736 Lin, Y. C., Tsai, C. J., Wu, Y. C., Zhang, R., Chi, K. H., Huang, Y. T., Lin, S. H., and Hsu, S. C.:
737 Characteristics of trace metals in traffic-derived particles in Hsuehshan Tunnel, Taiwan: size

738 distribution, potential source, and fingerprinting metal ratio, *Atmos. Chem. Phys.*, 15, 4117–4130,
739 <https://doi.org/10.5194/acp-15-4117-2015>, 2015.

740 Liu, B., Wu, J., Zhang, J., Wang, L., Yang, J., Liang, D., Dai, Q., Bi, X., Feng, Y., Zhang, Y., and Zhang,
741 Q.: Characterization and source apportionment of PM_{2.5} based on error estimation from EPA PMF
742 5.0 model at a medium city in China, *Environ. Pollut.*, 222, 10–22,
743 <https://doi.org/10.1016/j.envpol.2017.01.005>, 2017.

744 Madronich, S.: UV radiation in the natural and perturbed atmosphere, In: M. Tevini, Ed., *UV-B Radiation
745 and Ozone Depletion*, Lewis Publishers, London, pp. 17–69, 1993.

746 Malm William, C., Day Derek, E., Kreidenweis Sonia, M., Collett Jeffrey, L., and Lee, T.: Humidity-
747 dependent optical properties of fine particles during the Big Bend Regional Aerosol and Visibility
748 Observational Study, *J. Geophys. Res.-Atmos.*, 108(D9), 4279, doi:10.1029/2002JD002998, 2003.

749 Men, C., Liu, R., Xu, F., Wang, Q., Guo, L., and Shen, Z.: Pollution characteristics, risk assessment, and
750 source apportionment of heavy metals in road dust in Beijing, China, *Sci. Total Environ.*, 612, 138–
751 147, <https://doi.org/10.1016/j.scitotenv.2017.08.123>, 2018.

752 Milando, C., Huang, L., and Batterman, S.: Trends in PM_{2.5} emissions, concentrations and
753 apportionments in Detroit and Chicago, *Atmos. Environ.*, 129, 197–209,
754 <https://doi.org/10.1016/j.atmosenv.2016.01.012>, 2016.

755 National Bureau of Statistics (NBS): China Statistical Yearbook 2013, China Statistics Press, Beijing,
756 2013a (in Chinese).

757 Norris, G., Duvall, R., Brown, S., and Bai, S.: EPA Positive Matrix Factorization (PMF) 5.0 fundamentals
758 and User Guide Prepared for the US Environmental Protection Agency Office of Research and
759 Development, Washington, DC, Inc., Petaluma, 2014.

760 Paatero, P., and Tapper, U.: Positive matrix factorization: A non-negative factor model with optimal
761 utilization of error estimates of data values, *Environmetrics*, 5, 111–126,
762 <https://doi.org/10.1002/env.3170050203>, 2006.

763 Palancar, G. G., and Toselli, B. M.: Effects of meteorology and tropospheric aerosols on UV-B radiation:
764 a 4-year study, *Atmos. Environ.*, 38, 2749–2757, <https://doi.org/10.1016/j.atmosenv.2004.01.036>,
765 2004.

766 Pipal, A. S., Kulshrestha, A., and Taneja, A.: Characterization and morphological analysis of airborne
767 PM_{2.5} and PM₁₀ in Agra located in north central India, *Atmos. Environ.*, 45, 3621–3630,
768 <https://doi.org/10.1016/j.atmosenv.2011.03.062>, 2011.

769 Pitchford, M., Malm, W., Schichtel, B., Kumar, N., Lowenthal, D., and Hand, J.: Revised algorithm for
770 estimating light extinction from IMPROVE particle speciation data, *J. Air Waste Manage. Assoc.*,
771 57, 1326–1336, doi:10.3155/1047-3289.57.11.1326, 2007.

772 Pui, D. Y. H., Chen, S. C., and Zuo, Z. L.: PM_{2.5} in China: Measurements, sources, visibility and health
773 effects, and mitigation, *Particuology*, 13, 1–26, <https://doi.org/10.1016/j.partic.2013.11.001>, 2014.

774 Ran, L., Deng, Z. Z., Wang, P. C., and Xia, X. A.: Black carbon and wavelength-dependent aerosol
775 absorption in the North China Plain based on two-year aethalometer measurements, *Atmos. Environ.*,
776 142, 132–144, <https://doi.org/10.1016/j.atmosenv.2016.07.014>, 2016.

777 Sammaritano, M. A., Bustos, D. G., Poblete, A. G., and Wannaz, E. D.: Elemental composition of PM_{2.5}
778 in the urban environment of San Juan, Argentina, *Environ. Sci. Pollut. Res.*, 25, 4197–4203,
779 <https://doi.org/10.1007/s11356-017-0793-5>, 2018.

780 Sun, Y., Jiang, Q., Wang, Z., Fu, P., Li, J., Yang, T., and Yin, Y.: Investigation of the sources and
781 evolution processes of severe haze pollution in Beijing in January 2013, *J. Geophys. Res.-Atmos.*,
782 119, 4380–4398, doi:10.1002/2014JD021641, 2014.

783 Tang, G., Zhu, X., Hu, B., Xin, J., Wang, L., Münkel, C., Mao, G., and Wang, Y.: Impact of emission
784 controls on air quality in Beijing during APEC 2014: lidar ceilometer observations, *Atmos. Chem.*
785 *Phys.*, 15, 12667–12680, <https://doi.org/10.5194/acp-15-12667-2015>, 2015.

786 Tao, J., Gao, J., Zhang, L., Zhang, R., Che, H., Zhang, Z., Lin, Z., Jing, J., Cao, J., and Hsu, S. C.: PM_{2.5}
787 pollution in a megacity of southwest China: source apportionment and implication, *Atmos. Chem.*
788 *Phys.*, 14, 8679–8699, <https://doi.org/10.5194/acp-14-8679-2014>, 2014.

789 Tao, J., Gao, J., Zhang, L., Wang, H., Qiu, X., Zhang, Z., Wu, Y., Chai, F., and Wang, S.: Chemical and
790 optical characteristics of atmospheric aerosols in Beijing during the Asia-Pacific Economic
791 Cooperation China 2014, *Atmos. Environ.*, 144, 8–16,
792 <https://doi.org/10.1016/j.atmosenv.2016.08.067>, 2016.

793 Tao, J., Zhang, L. M., Cao, J. J., and Zhang, R. J.: A review of current knowledge concerning PM_{2.5}
794 chemical composition, aerosol optical properties and their relationships across China, *Atmos. Chem.*
795 *Phys.*, 17, 9485–9518, <https://doi.org/10.5194/acp-17-9485-2017>, 2017.

796 Tie, X., Huang, R.-J., Dai, W., Cao, J., Long, X., Su, X., Zhao, S., Wang, Q., and Li, G.: Effect of heavy
797 haze and aerosol pollution on rice and wheat productions in China, *Sci. Rep.*, 6, 29612,
798 doi:10.1038/srep29612, 2016.

799 Wang, J., Wang, G., Gao, J., Wang, H., Ren, Y., Li, J., Zhou, B., Wu, C., Zhang, L., Wang, S., and Chai,
800 F.: Concentrations and stable carbon isotope compositions of oxalic acid and related SOA in Beijing
801 before, during, and after the 2014 APEC, *Atmos. Chem. Phys.*, 17, 981–992,
802 <https://doi.org/10.5194/acp-17-981-2017>, 2017.

803 Wang, Q. Q., He, X., Huang, X. H. H., Griffith, S. M., Feng, Y., Zhang, T., Zhang, Q., Wu, D., and Yu,
804 J. Z.: Impact of secondary organic aerosol tracers on tracer-based source apportionment of organic
805 carbon and PM_{2.5}: A case study in the Pearl River Delta, China, *Earth and Space Chemistry*, 1, 562–
806 571, doi:10.1021/acsearthspacechem.7b00088, 2017.

807 Wang, Q. Y., Huang, R.-J., Cao, J., Tie, X., Shen, Z., Zhao, S., Han, Y., Li, G., Li, Z., Ni, H., Zhou, Y.,
808 Wang, M., Chen, Y., and Su, X.: Contribution of regional transport to the black carbon aerosol during
809 winter haze period in Beijing, *Atmos. Environ.*, 132, 11–18,
810 <http://dx.doi.org/10.1016/j.atmosenv.2016.02.031>, 2016a.

811 Wang, Q. Y., Huang, R.-J., Zhao, Z., Cao, J., Ni, H., Tie, X., Zhao, S., Su, X., Han, Y., Shen, Z., Wang,
812 Y., Zhang, N., Zhou, Y., and Corbin, J. C.: Physicochemical characteristics of black carbon aerosol
813 and its radiative impact in a polluted urban area of China, *J. Geophys. Res.-Atmos.*, 121, 12505–
814 12519, doi:10.1002/2016JD024748, 2016b.

815 Wang, Q. Y., Cao, J., Han, Y., Tian, J., Zhang, Y., Pongpiachan, S., Zhang, Y., Li, L., Niu, X., Shen, Z.,
816 Zhao, Z., Tipmanee, D., Bunsomboonsakul, S., Chen, Y., and Sun, J.: Enhanced light absorption due
817 to the mixing state of black carbon in fresh biomass burning emissions, *Atmos. Environ.*, 180, 184–
818 191, <https://doi.org/10.1016/j.atmosenv.2018.02.049>, 2018a.

819 Wang, Q. Y., Cao, J., Han, Y., Tian, J., Zhu, C., Zhang, Y., Zhang, N., Shen, Z., Ni, H., Zhao, S., and
820 Wu, J.: Sources and physicochemical characteristics of black carbon aerosol from the southeastern
821 Tibetan Plateau: internal mixing enhances light absorption, *Atmos. Chem. Phys.*, 18, 4639–4656,
822 <https://doi.org/10.5194/acp-18-4639-2018>, 2018b.

823 Wang, S., Zhao, M., Xing, J., Wu, Y., Zhou, Y., Lei, Y., He, K., Fu, L., and Hao, J.: Quantifying the air
824 pollutants emission reduction during the 2008 Olympic Games in Beijing, *Environ. Sci. Technol.*,
825 44, 2490–2496, doi:10.1021/es9028167, 2010.

826 Wang, W., Primbs, T., Tao, S., and Simonich, S. L. M.: Atmospheric particulate matter pollution during
827 the 2008 Beijing Olympics, *Environ. Sci. Technol.*, 43, 5314–5320, doi:10.1021/es9007504, 2009.

- 828 Wang, Z., Li, Y., Chen, T., Li, L., Liu, B., Zhang, D., Sun, F., Wei, Q., Jiang, L., and Pan, L.: Changes
829 in atmospheric composition during the 2014 APEC conference in Beijing, *J. Geophys. Res.-Atmos.*,
830 120, 12695–12707, doi:10.1002/2015JD023652, 2015.
- 831 Watson, J. G.: Visibility: Science and regulation, *J. Air Waste Manage. Assoc.*, 52, 628–713,
832 <https://doi.org/10.1080/10473289.2002.10470813>, 2002.
- 833 Xia, X., Li, Z., Wang, P., Chen, H., and Cribb, M.: Estimation of aerosol effects on surface irradiance
834 based on measurements and radiative transfer model simulations in northern China, *J. Geophys.*
835 *Res.- Atmos.*, 112, D22S10, doi:10.1029/2006JD008337, 2007a.
- 836 Xia, X., Li, Z., Holben, B., Wang, P., Eck, T., Chen, H., Cribb, M., and Zhao, Y.: Aerosol optical
837 properties and radiative effects in the Yangtze Delta region of China, *J. Geophys. Res.- Atmos.*, 112,
838 D22S12, doi:10.1029/2007JD008859, 2007b.
- 839 Xiao, S., Wang, Q., Cao, J., Huang, R.-J., Chen, W., Han, Y., Xu, H., Liu, S., Zhou, Y., and Wang, P.:
840 Long-term trends in visibility and impacts of aerosol composition on visibility impairment in Baoji,
841 China, *Atmos. Res.*, 149, 88–95, <http://dx.doi.org/10.1016/j.atmosres.2014.06.006>, 2014.
- 842 Xie, R., Sabel, C. E., Lu, X., Zhu, W. M., Kan, H. D., Nielsen, C. P., and Wang, H. K.: Long-term trend
843 and spatial pattern of PM_{2.5} induced premature mortality in China, *Environ. Int.*, 97, 180–186,
844 <https://doi.org/10.1016/j.envint.2016.09.003>, 2016.
- 845 Xu, H. M., Cao, J. J., Ho, K. F., Ding, H., Han, Y. M., Wang, G. H., Chow, J. C., Watson, J. G., Khol, S.
846 D., Qiang, J., and Li, W. T.: Lead concentrations in fine particulate matter after the phasing out of
847 leaded gasoline in Xi'an, China, *Atmos. Environ.*, 46, 217–224,
848 <https://doi.org/10.1016/j.atmosenv.2011.09.078>, 2012.
- 849 Xu, J., Bergin, M. H., and Greenwald, R.: Direct aerosol radiative forcing in the Yangtze delta region of
850 China: Observation and model estimation, *J. Geophys. Res.-Atmos.*, 108(D2), 4060,
851 doi:10.1029/2002JD002550, 2003.
- 852 Xu, W., Song, W., Zhang, Y., Liu, X., Zhang, L., Zhao, Y., Liu, D., Tang, A., Yang, D., Wang, D., Wen,
853 Z., Pan, Y., Fowler, D., Collett Jr, J. L., Erisman, J. W., Goulding, K., Li, Y., and Zhang, F.: Air
854 quality improvement in a megacity: implications from 2015 Beijing Parade Blue pollution control
855 actions, *Atmos. Chem. Phys.*, 17, 31–46, <https://doi.org/10.5194/acp-17-31-2017>, 2017.
- 856 Xu, W. Q., Sun, Y. L., Chen, C., Du, W., Han, T. T., Wang, Q. Q., Fu, P. Q., Wang, Z. F., Zhao, X. J.,
857 Zhou, L. B., Ji, D. S., Wang, P. C., and Worsnop, D. R.: Aerosol composition, oxidation properties,
858 and sources in Beijing: results from the 2014 Asia-Pacific Economic Cooperation summit study,
859 *Atmos. Chem. Phys.*, 15, 13681–13698, <https://doi.org/10.5194/acp-15-13681-2015>, 2015.
- 860 Yang, M., Howell, S. G., Zhuang, J., and Huebert, B. J.: Attribution of aerosol light absorption to black
861 carbon, brown carbon, and dust in China—interpretations of atmospheric measurements during EAST-
862 AIRE, *Atmos. Chem. Phys.*, 9, 2035–2050, <https://doi.org/10.5194/acp-9-2035-2009>, 2009.
- 863 Zhang, R., Jing, J., Tao, J., Hsu, S. C., Wang, G., Cao, J., Lee, C. S. L., Zhu, L., Chen, Z., Zhao, Y., and
864 Shen, Z.: Chemical characterization and source apportionment of PM_{2.5} in Beijing: seasonal
865 perspective, *Atmos. Chem. Phys.*, 13, 7053–7074, doi:10.5194/acp-13-7053-2013, 2013.
- 866 Zhang, T., Cao, J. J., Tie, X. X., Shen, Z. X., Liu, S. X., Ding, H., Han, Y. M., Wang, G. H., Ho, K. F.,
867 Qiang, J., and Li, W. T.: Water-soluble ions in atmospheric aerosols measured in Xi'an, China:
868 Seasonal variations and sources, *Atmos. Res.*, 102, 110–119,
869 <https://doi.org/10.1016/j.atmosres.2011.06.014>, 2011.
- 870 Zhang, Y., Lang, J., Cheng, S., Li, S., Zhou, Y., Chen, D., Zhang, H., and Wang, H.: Chemical
871 composition and sources of PM₁ and PM_{2.5} in Beijing in autumn, *Sci. Total Environ.*, 630, 72–82,
872 <https://doi.org/10.1016/j.scitotenv.2018.02.151>, 2018.

- 873 Zheng, G., Duan, F., Ma, Y., Zhang, Q., Huang, T., Kimoto, T., Cheng, Y., Su, H., and He, K.: Episode-
874 based evolution pattern analysis of haze pollution: Method development and results from Beijing,
875 China, *Environ. Sci. Technol.*, 50, 4632–4641, doi:10.1021/acs.est.5b05593, 2016.
- 876 Zheng, G. J., Duan, F. K., Su, H., Ma, Y. L., Cheng, Y., Zheng, B., Zhang, Q., Huang, T., Kimoto, T.,
877 Chang, D., Pöschl, U., Cheng, Y. F., and He, K. B.: Exploring the severe winter haze in Beijing: the
878 impact of synoptic weather, regional transport and heterogeneous reactions, *Atmos. Chem. Phys.*,
879 15, 2969–2983, <https://doi.org/10.5194/acp-15-2969-2015>, 2015.
- 880 Zhong, J., Zhang, X., Dong, Y., Wang, Y., Liu, C., Wang, J., Zhang, Y., and Che, H.: Feedback effects
881 of boundary-layer meteorological factors on cumulative explosive growth of PM_{2.5} during winter
882 heavy pollution episodes in Beijing from 2013 to 2016, *Atmos. Chem. Phys.*, 18, 247–258,
883 <https://doi.org/10.5194/acp-18-247-2018>, 2018.
- 884 Zong, Z., Wang, X., Tian, C., Chen, Y., Qu, L., Ji, L., Zhi, G., Li, J., and Zhang, G.: Source apportionment
885 of PM_{2.5} at a regional background site in North China using PMF linked with radiocarbon analysis:
886 insight into the contribution of biomass burning, *Atmos. Chem. Phys.*, 16, 11249–11265,
887 <https://doi.org/10.5194/acp-16-11249-2016>, 2016.
- 888 Zhou, Y., Wang, Q., Huang, R., Liu, S., Tie, X., Su, X., Niu, X., Zhao, Z., Ni, H., Wang, M., Zhang, Y.,
889 and Cao, J.: Optical properties of aerosols and implications for radiative effects in Beijing during the
890 Asia-Pacific Economic Cooperation Summit 2014, *J. Geophys. Res.-Atmos.*, 122, 10119–10132,
891 <https://doi.org/10.1002/2017JD026997>, 2017.
- 892 Zhuang, B. L., Wang, T. J., Liu, J., Li, S., Xie, M., Yang, X. Q., Fu, C. B., Sun, J. N., Yin, C. Q., Liao, J.
893 B., Zhu, J. L., and Zhang, Y.: Continuous measurement of black carbon aerosol in urban Nanjing of
894 Yangtze River Delta, China, *Atmos. Environ.*, 89, 415–424,
895 <https://doi.org/10.1016/j.atmosenv.2014.02.052>, 2014.

896

897

Table 1 Summary of PM_{2.5} and its major chemical components at Xianghe during the 19th

898

National Congress of the Communist Party of China (NCCPC)-control and non-control periods.

| Components | Grand average ($\mu\text{g m}^{-3}$) | Control period ($\mu\text{g m}^{-3}$) | Non-control period ($\mu\text{g m}^{-3}$) | Change ratio ^a (%) |
|-------------------------------|-------------------------------------------|--------------------------------------------|------------------------------------------------|----------------------------------|
| PM _{2.5} | 70.0 | 57.9 (63.7) ^b | 84.1 (112.6) | 31.2 (43.4) |
| NO ₃ ⁻ | 15.0 | 13.4 (18.0) | 16.9 (24.3) | 20.7 (25.9) |
| SO ₄ ²⁻ | 5.6 | 5.8 (7.6) | 5.3 (6.6) | -9.4 (-15.2) |
| NH ₄ ⁺ | 6.0 | 5.4 (8.6) | 6.8 (9.7) | 20.6 (11.3) |
| Cl ⁻ | 2.2 | 1.6 (1.5) | 2.9 (3.4) | 44.8 (55.9) |
| Organic matter | 18.9 | 14.0 (9.5) | 24.6 (29.8) | 43.1 (68.1) |
| Elemental carbon | 5.2 | 4.5 (4.5) | 6.0 (7.5) | 25.0 (40.0) |
| Trace elements | 1.8 | 1.4 (1.2) | 2.3 (3.0) | 39.1 (60.0) |
| Fine soil | 5.5 | 4.2 (2.6) | 7.1 (6.3) | 40.8 (58.7) |

899

^a([Non-control period]-[NCCPC-control period])/[Non-control period].

900

^bValues in parentheses show the results for days with stable meteorological conditions (wind speed < 0.4 m s⁻¹ and mixed layer height < 274 m).

901

902

Figure Captions

904 **Figure 1.** Location of the Xianghe sampling site. The map was drawn using the ArcGIS.

905 **Figure 2.** (left) Daily variations in the contributions of chemical species to PM_{2.5} mass during the
906 campaign and (right) average contributions of chemical species during the 19th National Congress
907 of the Communist Party of China (NCCPC)-control and non-control periods. PE1 and PE2 represent
908 two pollution episodes.

909 **Figure 3.** Scatter plots showing the relationships between PM_{2.5} mass concentrations and (a) wind speed
910 and (b) mixed layer height.

911 **Figure 4.** (a) Source profiles for the six sources identified using the positive matrix factorization model
912 version 5.0, (b) the mass concentrations of PM_{2.5} contributed by each source, and (c) the average
913 source contribution of each source to the PM_{2.5} mass.

914 **Figure 5.** Average source contributions of (a) each positive matrix factorization source factor and (b)
915 chemical species to the PM_{2.5} mass during two pollution episodes (PE1 and PE2).

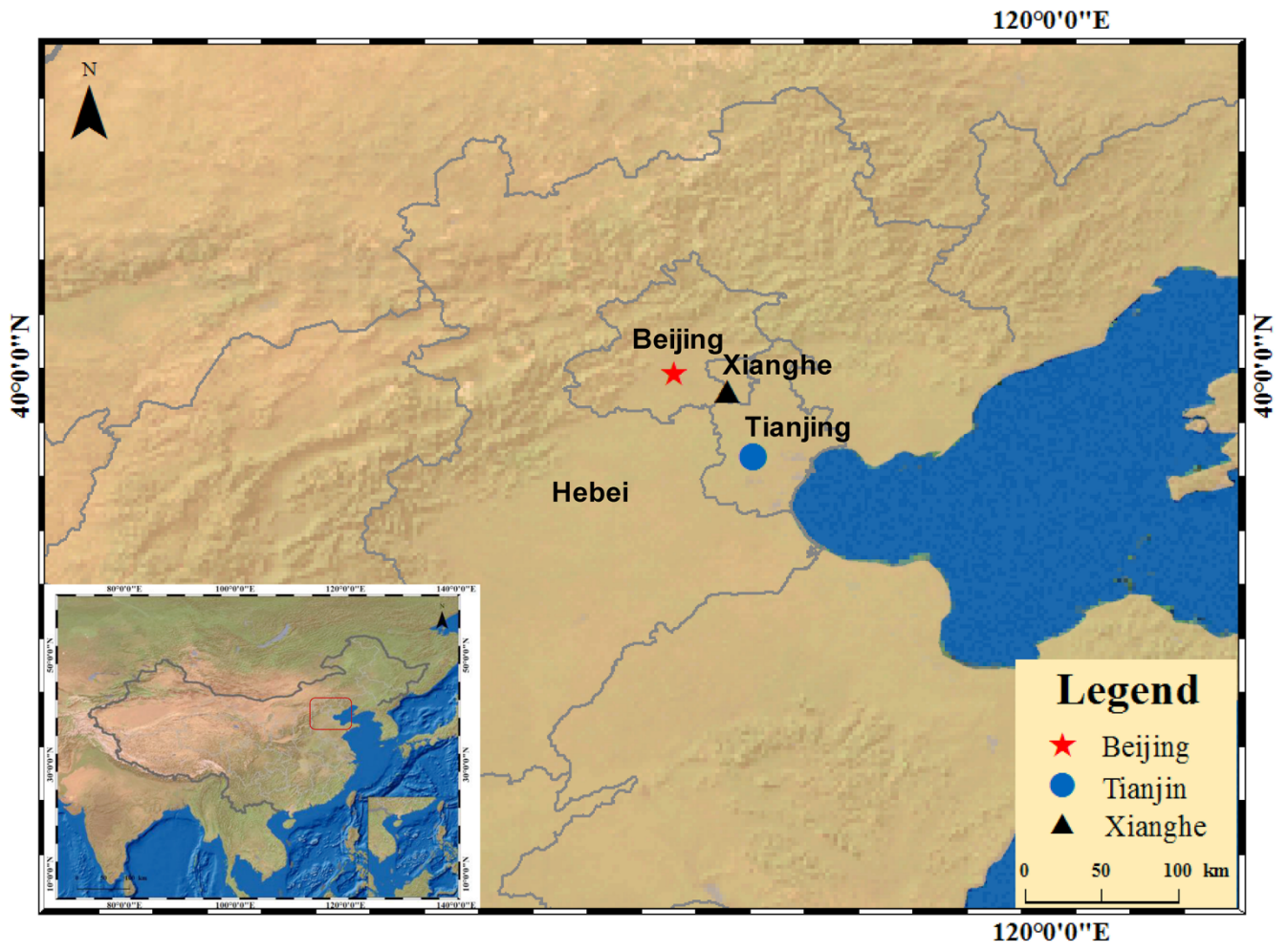
916 **Figure 6.** Correlations for (a) PM_{2.5} mass concentrations versus molar ratios of NO₃⁻ and NO₂ (NOR), (b)
917 NOR versus relative humidity (RH), (c) the ratio of secondary organic aerosol to elemental carbon
918 (SOA/EC) ratios versus Ox (O₃ + NO₂), and (d) SOA/EC versus RH for all samples from the
919 campaign.

920 **Figure 7.** Three-day backward in time air mass trajectories (BT) arriving at 150 m above ground every
921 hour from 31 October to 1 November 2017. The orange points represent fire counts that were derived
922 from Moderate Resolution Imaging Spectroradiometer observations.

923 **Figure 8.** Surface weather charts for 08:00 (local time) over East Asia from 22 October to 2 November
924 2017. The black triangles represent Xianghe.

925 **Figure 9.** Daily average PM_{2.5} concentrations (μg m⁻³) simulated for the Beijing-Tianjin-Hebei region
926 and surrounding areas from 25 October to 2 November 2017. The Weather Research and Forecasting
927 model coupled to chemistry (WRF-Chem) model was used for the simulation.

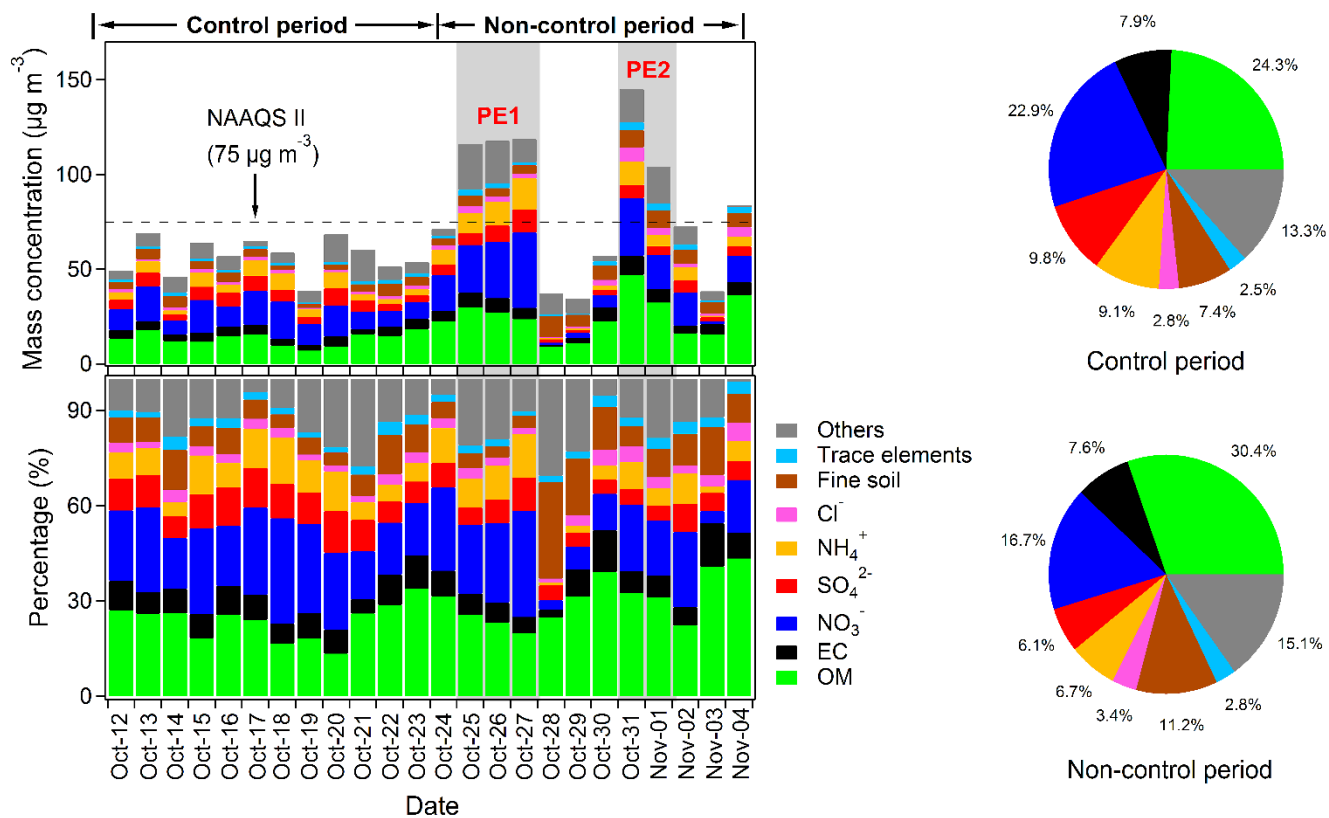
928 **Figure 10.** Average values of (a) light extinction coefficients (including light scattering and absorption)
929 and (b) direct radiative forcing (DRF) at the surface contributed by each PM_{2.5} chemical composition
930 during the 19th National Congress of the Communist Party of China (NCCPC)-control and non-
931 control periods.



933

934

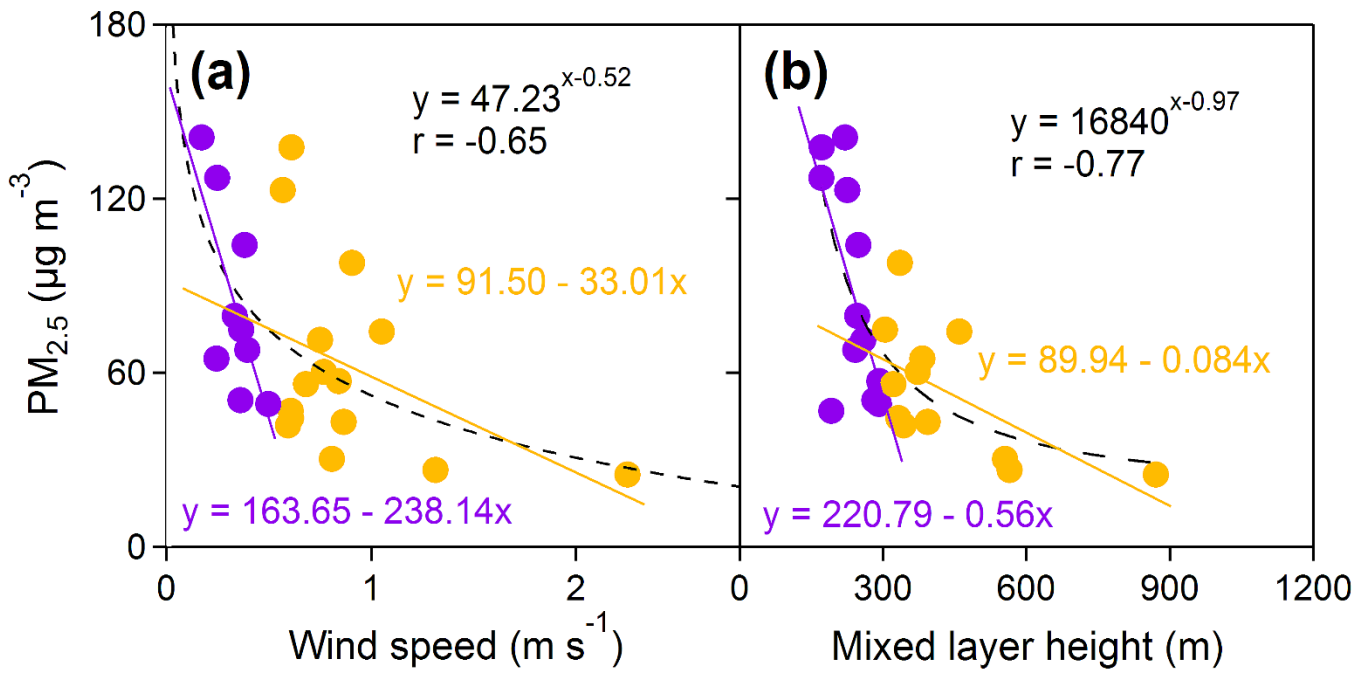
935 **Figure 1.**



936

937 **Figure 2.**

938

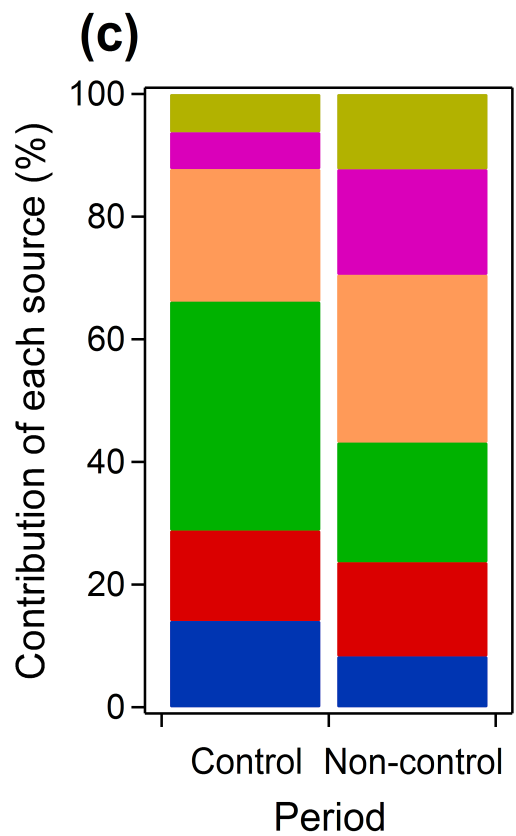
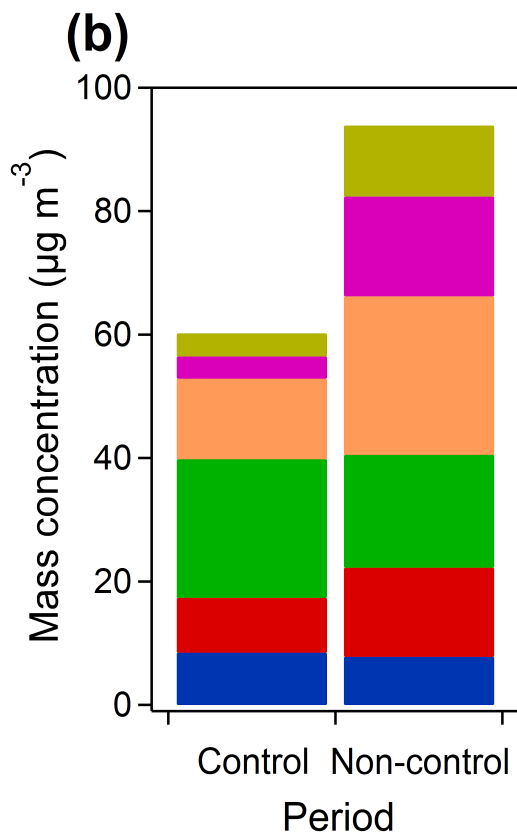
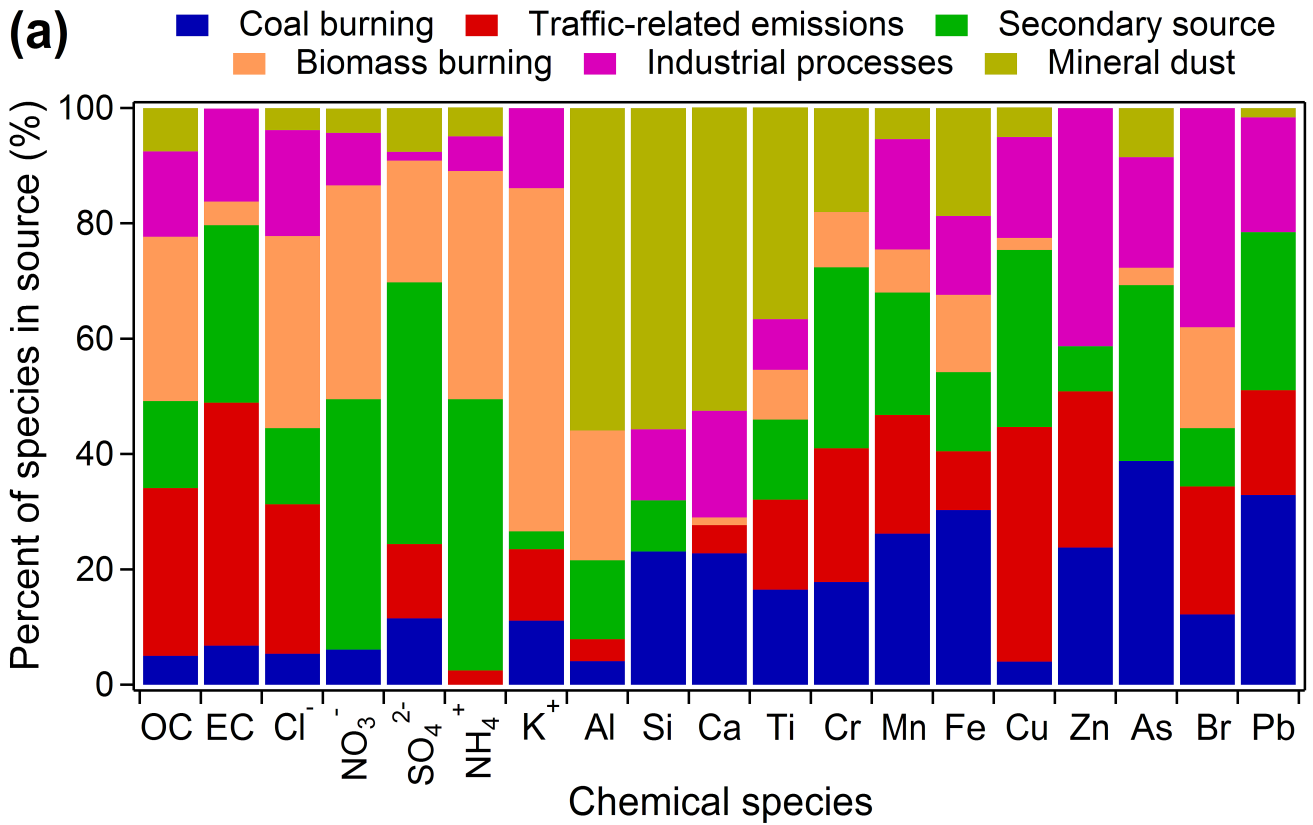


939

940

941 **Figure 3.**

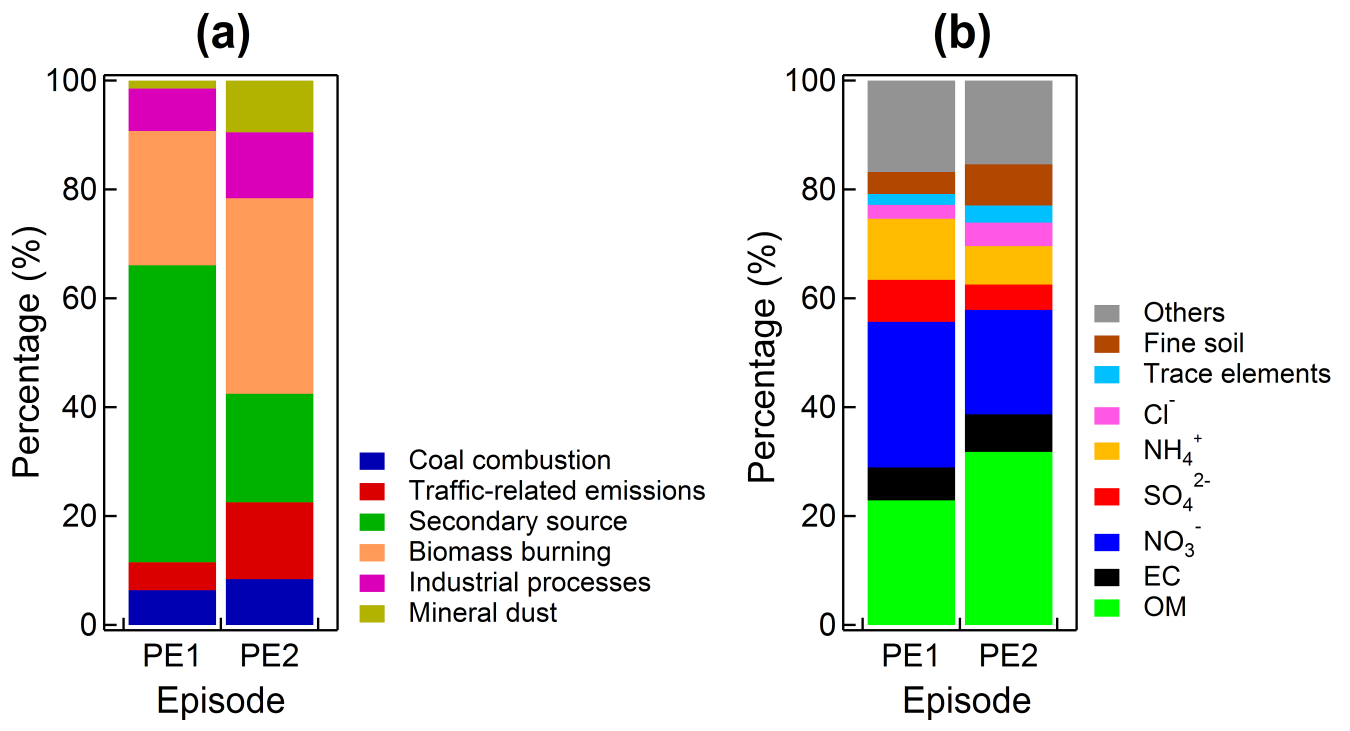
942



943

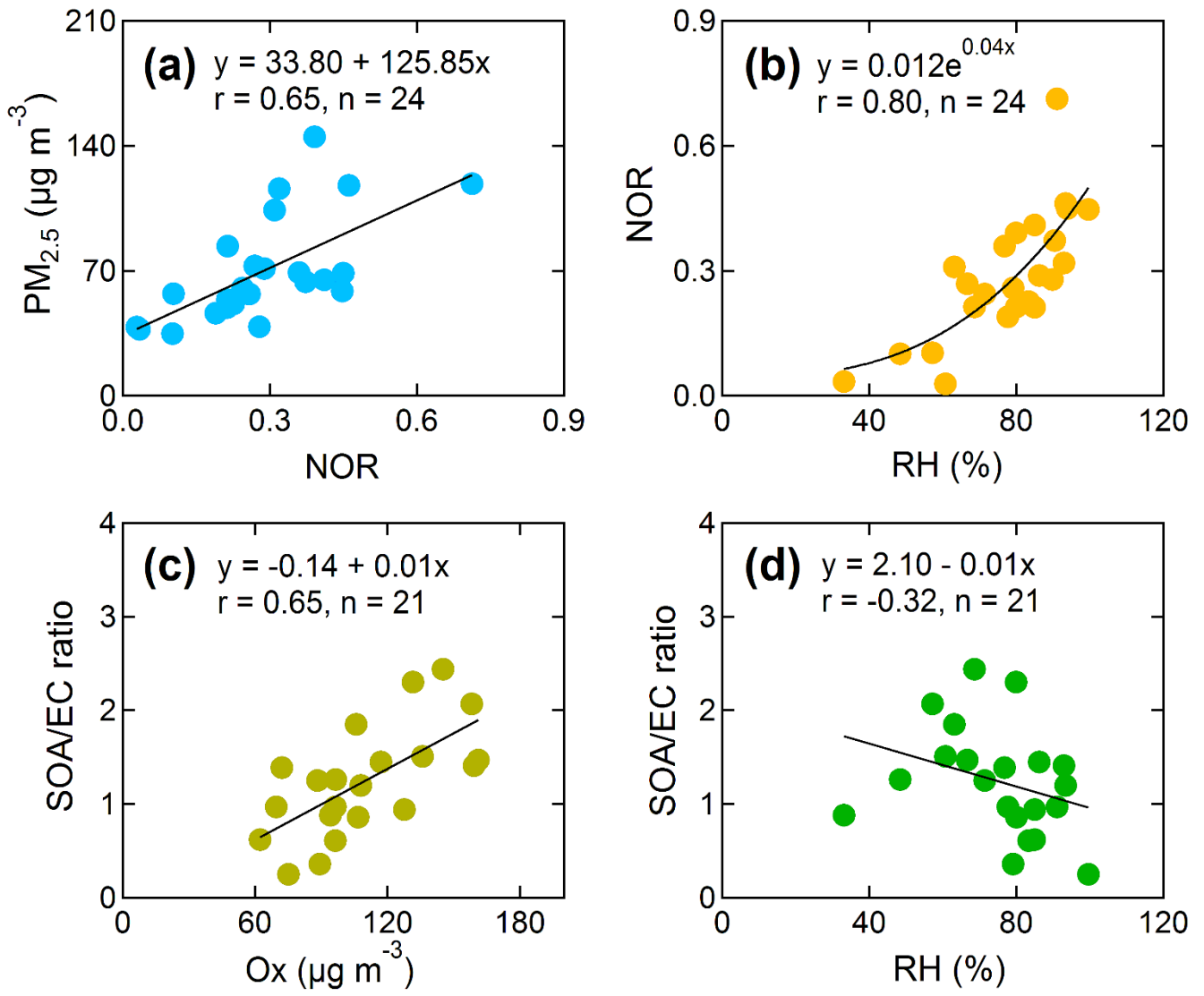
944

945 **Figure 4.**



946
947
948
949

Figure 5.

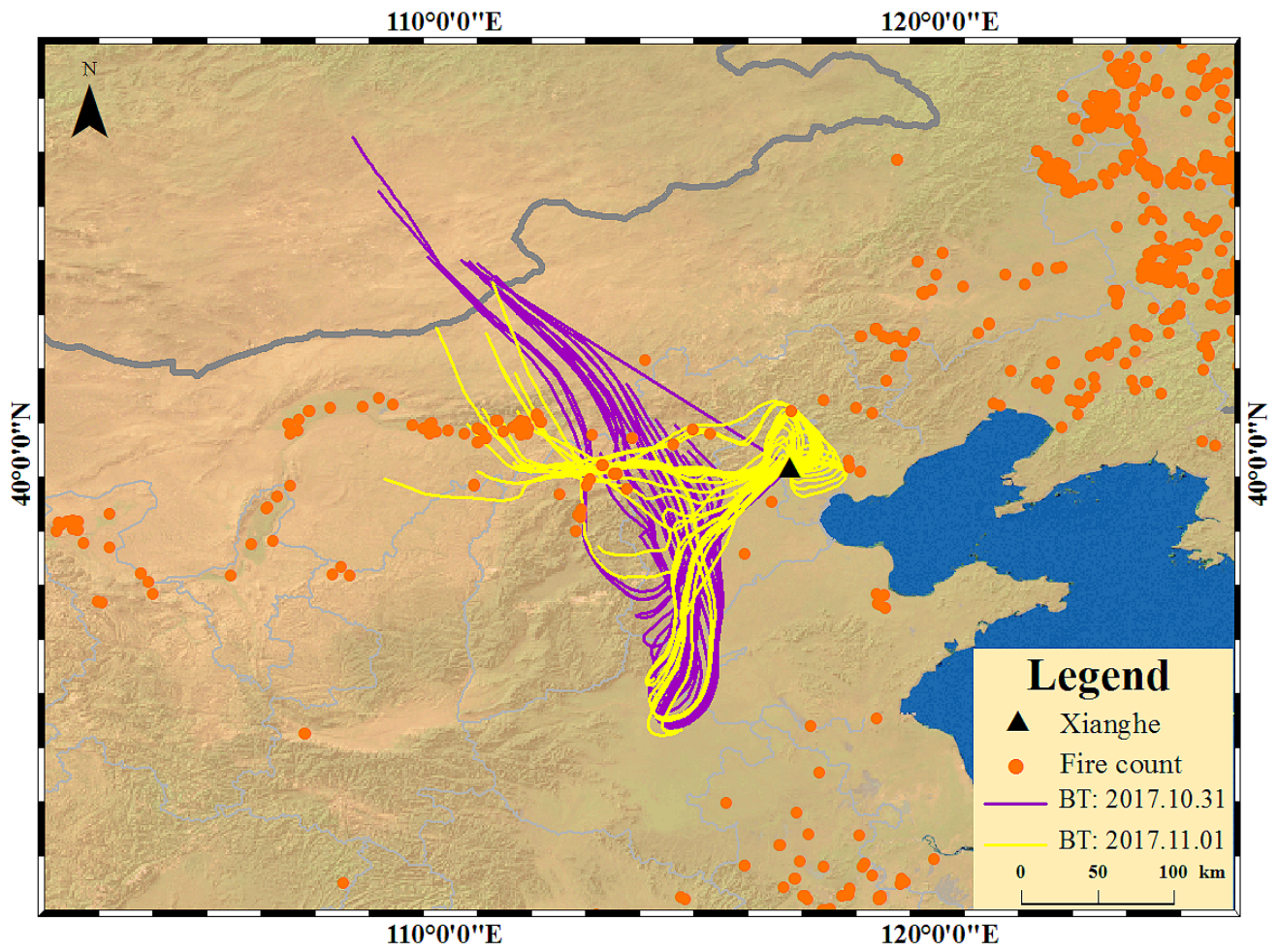


950

951

952 **Figure 6.**

953

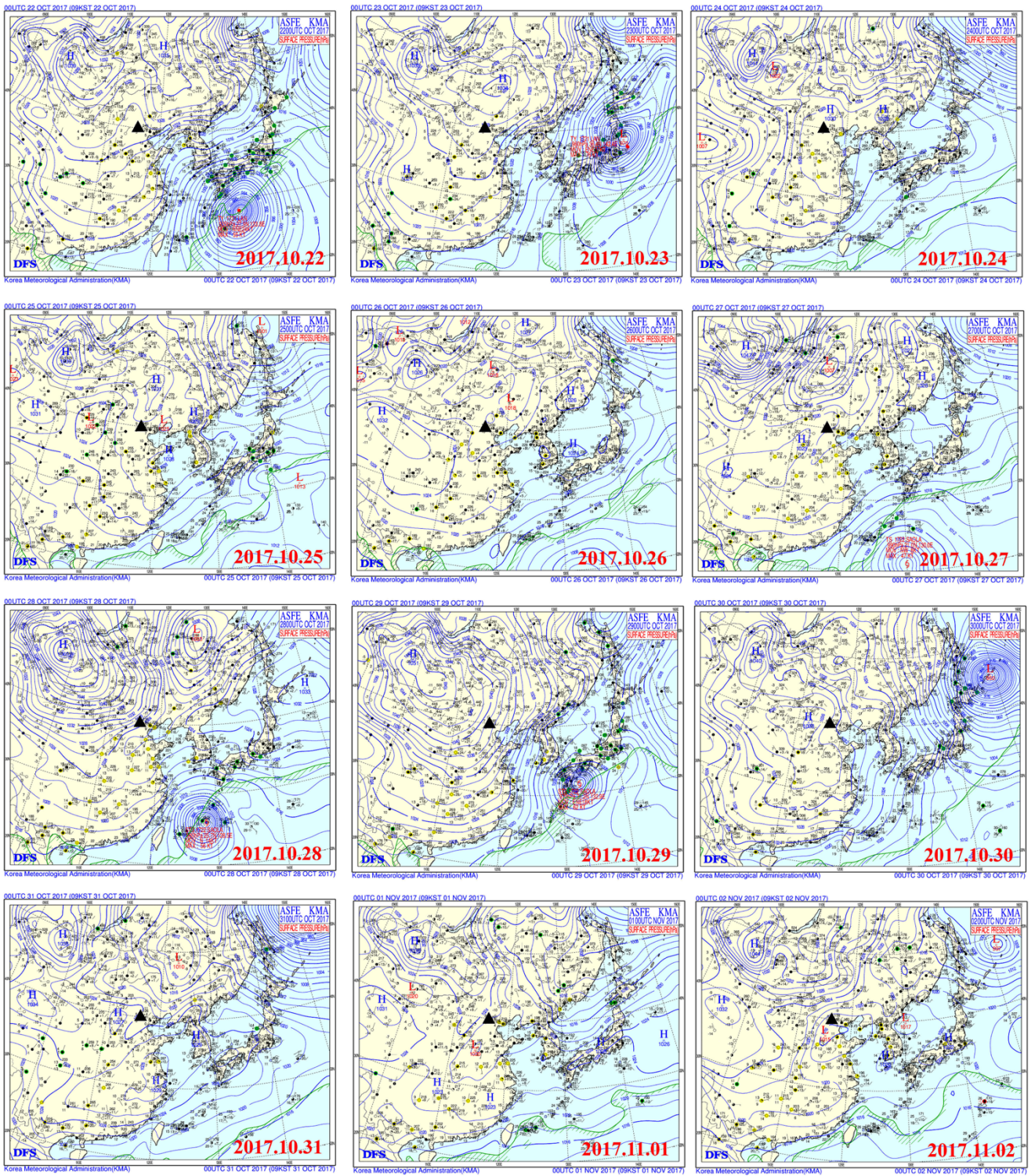


954

955

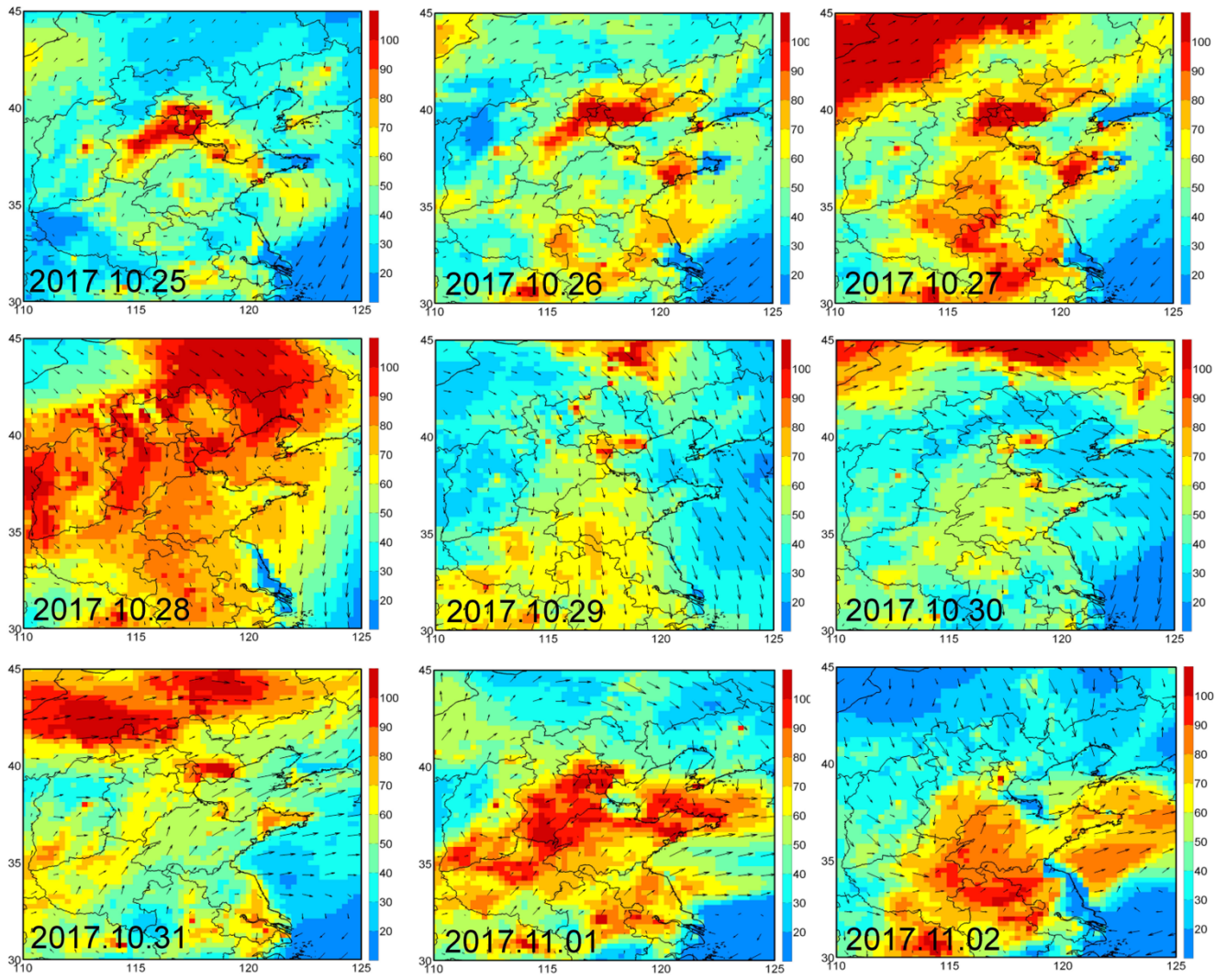
956 **Figure 7.**

957



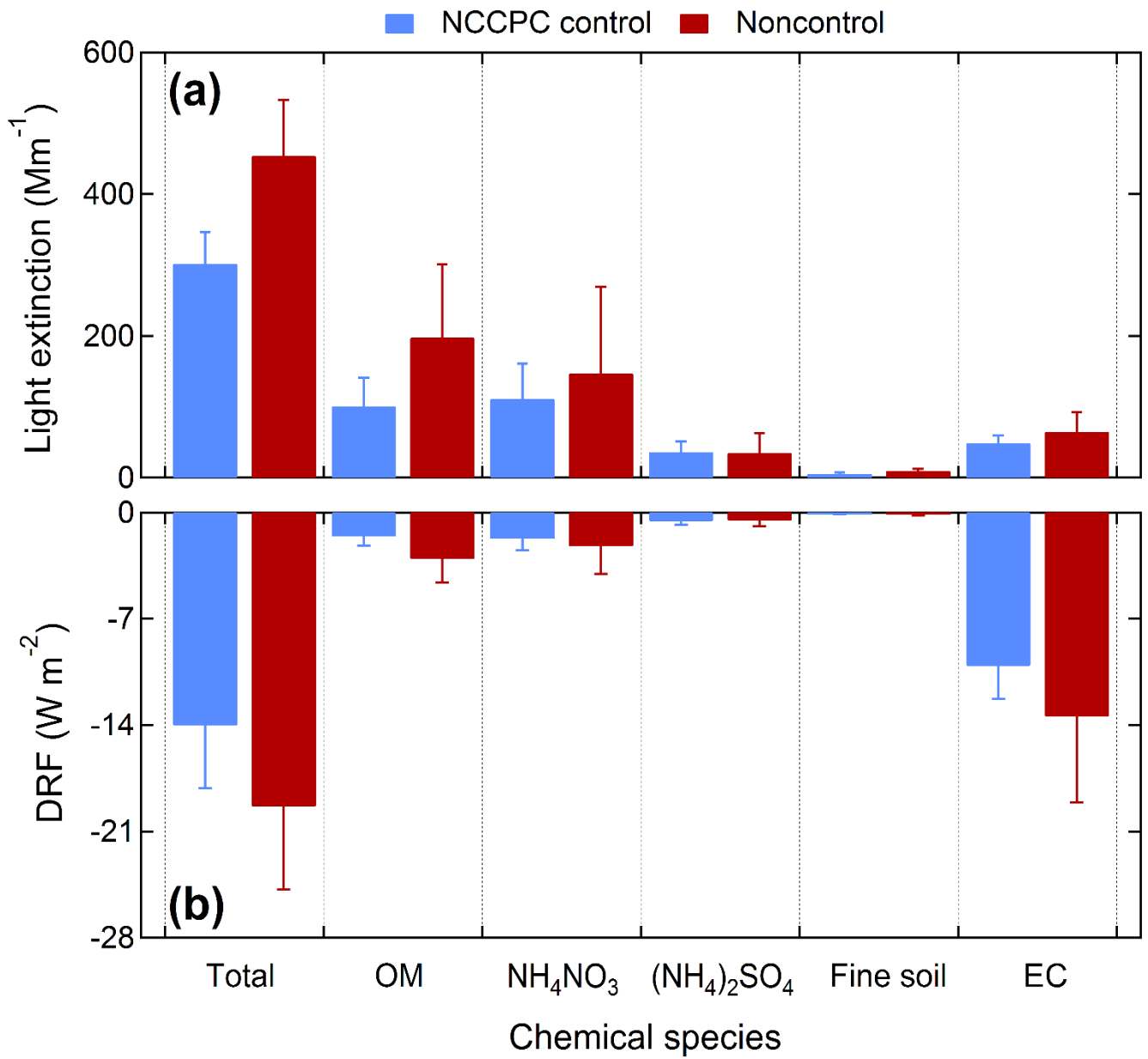
958
 959
 960
 961

Figure 8.



962
 963
 964
 965

Figure 9.



966

967

968 **Figure 10.**